









SN 2020sck: Deflagration in a Carbon-Oxygen White Dwarf

Anirban Dutta^{1,2} , D. K. Sahu¹ , G. C. Anupama¹ , Simran Joharle³, Brajesh Kumar⁴ , Nayana A J¹, Avinash Singh⁵ ,
Harsh Kumar^{6,7}, Varun Bhalerao⁶ , and Sudhansu Barway⁴

¹ Indian Institute of Astrophysics, II Block, Koramangala, Bangalore 560034, India; anirban.dutta@iiap.res.in, anirbaniamdutta@gmail.com

² Pondicherry University, R.V. Nagar, Kalapet, 605014, Puducherry, India

³ Department of Physics, Fergusson College, Autonomous, Pune, India

⁴ Aryabhata Research Institute of Observational Sciences, Manora Peak, Nainital 263 001, India

⁵ Hiroshima Astrophysical Science Center, Hiroshima University, Higashi-Hiroshima, Hiroshima 739-8526, Japan

⁶ Department of Physics, Indian Institute of Technology, Bombay, Powai, Mumbai 400076, India

Received 2021 September 8; revised 2021 October 29; accepted 2021 November 1; published 2022 February 7

Abstract

We present optical *UBVRI* photometry and low-to-medium resolution spectroscopic observations of type Iax supernova SN 2020sck spanning -5.5 days to $+67$ days from maximum light in the *B*-band. From the photometric analysis we find $\Delta m_B(15) = 2.03 \pm 0.05$ mag and $M_B = -17.81 \pm 0.22$ mag. Radiation diffusion model fit to the quasi-bolometric light curve indicates $0.13 \pm 0.02 M_\odot$ of ^{56}Ni and $0.34 M_\odot$ of ejecta are synthesized in the explosion. Comparing the observed quasi-bolometric light curve with the angle-averaged bolometric light curve of a three-dimensional pure deflagration explosion of M_{ch} carbon-oxygen white dwarf, we find agreement with a model in which $0.16 M_\odot$ of ^{56}Ni and $0.37 M_\odot$ of ejecta is formed. By comparing the $+1.4$ days spectrum of SN 2020sck with synthetic spectrum generated using SYN++, we find absorption features due to C II, C III, and O I. These are unburned materials in the explosion and indicate a C–O white dwarf. One-dimensional radiative transfer modeling of the spectra with TARDIS shows higher density in the ejecta near the photosphere and a steep decrease in the outer layers with an ejecta composition dominated mostly by C, O, Si, Fe, and Ni. The star-formation rate of the host galaxy computed from the luminosity of the $\text{H}\alpha$ ($\lambda 6563$) line is $0.09 M_\odot \text{yr}^{-1}$, indicating a relatively young stellar environment.

Unified Astronomy Thesaurus concepts: [Supernovae \(1668\)](#)

Supporting material: data behind figure

1. Introduction

Thermonuclear supernovae, also known as type Ia supernovae (SNe Ia), result from the thermonuclear explosion of degenerate carbon-oxygen (C–O) white dwarf that accretes matter from a companion star (Hoyle & Fowler 1960; Wang & Han 2012; Maeda & Terada 2016). There exists a tight correlation between luminosity at maximum light and light curve decline rate for normal SNe Ia, with brighter objects having broader light curves (Phillips et al. 1999). This points toward the fact that SNe Ia form a homogeneous class of objects. But, observations have revealed that there exists significant diversity that could be due to the progenitor systems and/or the explosion mechanisms (Maoz et al. 2014; Taubenberger 2017). One such peculiar subclass of thermonuclear origin is the Iax type (SNe Iax). SN 2002cx was the first of this kind studied in detail (Li et al. 2003; Jha et al. 2006).

The most important distinguishing feature of SNe Iax is their low expansion velocity of 2000 (SN 2008ha, Foley et al. 2009)–8000 km s^{-1} (SN 2012Z, Stritzinger et al. 2014) as compared to SNe Ia ($v \sim 11,000 \text{ km s}^{-1}$, Wang et al. 2009; Foley et al. 2013), measured from the absorption minimum of the P-Cygni profiles. Their premaximum spectra are similar to SN 1991T-like objects. The spectra are dominated by ions of

C II, C III, and O I, intermediate mass elements (IMEs) like Mg II, Si II, Si III, S II, Ca II, Sc II, and Ti II, and also Fe-group elements (IGEs) like Fe II, Fe III, Co II, and Co III. The late time spectra are dominated with permitted Fe II lines with low expansion velocities (Jha et al. 2006; Sahu et al. 2008). This indicates that the inner regions of the ejecta in SNe Iax have a higher density compared to normal SNe Ia.

SNe Iax tend to be less luminous compared to SNe Ia (~ -19.3 mag). The peak optical luminosity spans a wide range from $M_V = -18.4$ mag (Narayan et al. 2011) to $M_g = -13.8$ mag (Srivastav et al. 2020). The *I*-band light curve does not show the secondary maximum, typically seen in SNe Ia caused either due to higher ionization of the absorption lines of Fe and Co (Kasen 2006) or strong mixing in the ejecta, which reduces the Fe-peak elements in the central region (Blinnikov et al. 2006). The $(B - V)$, $(V - R)$, and $(V - I)$ color curves show significant scatter, which can be related to host galaxy reddening or intrinsic to the SN itself (Foley et al. 2013).

Several progenitor systems and their variants have been proposed to understand the nature of the explosion of SNe Ia. Among them, the single-degenerate (SD; Whelan & Iben 1973; Nomoto 1982a, 1982b; Nomoto & Leung 2018) and the double-degenerate (DD, Iben & Tutukov 1984; Webbink 1984; Tanikawa et al. 2018, 2019) scenarios can explain a range of observed properties of SNe Ia. The WD accretes matter from a non-degenerate companion star (main-sequence, red-giant, He star) for the SD scenario. In the DD case, the explosion occurs when two white dwarfs merge. Another possible progenitor scenario is core-degenerate (CD; Sparks & Stecher 1974; Soker 2015), which is a result of the merger of a white dwarf with an asymptotic giant branch (AGB) star.

⁷ LSSTC DSFP Fellow 2018.

There have been a few studies to understand the progenitors of SNe Iax. A blue progenitor was detected for SN 2012Z in deep pre-explosion Hubble Space Telescope (HST) images (McCully et al. 2014, 2021). The colors and luminosity indicated the progenitor to be a white dwarf accreting matter from a helium star. In the case of SN 2004cs and SN 2007J, He I emission feature was detected in their post-maximum spectrum (Foley et al. 2009, 2013), which was explained as being due to a C–O white dwarf accreting matter from a He-donor, or as a result of interaction with circumstellar material (Foley et al. 2009). However, in the case of SN 2007J, the large helium content ($\sim 0.01 M_{\odot}$) challenges the helium shell accretion scenario on a M_{ch} white dwarf (Magee et al. 2019). A source consistent with the position of SN 2008ha was detected in the post-explosion HST image, which could be the progenitor white dwarf remnant after the explosion, or the companion star. This source is redder than the progenitor of SN 2012Z (Foley et al. 2014). Valenti et al. (2009) proposed weak explosions due to the core collapse of massive stars such as Wolf–Rayet stars as the progenitor of SN 2008ha. These stars, due to their high mass-loss rate, are hydrogen deficient. Most massive star progenitor scenarios were rejected as progenitors for SN 2008ge from the star formation rate of the host galaxy (Foley et al. 2010b). Using pre-explosion HST images for SN 2014dt, Foley et al. 2015 ruled out red giant or horizontal branch stars ($M_{\text{initial}} \geq 8 M_{\odot}$) and massive main-sequence stars ($M_{\text{initial}} \geq 16 M_{\odot}$) as progenitors. SN 2014dt shows mid-IR flux excess consistent with emission from newly formed dust. The derived mass-loss rate is consistent with either a red-giant or an AGB star (Fox et al. 2016).

There is a range of explosion models proposed to explain the observed diversity of SNe Ia. The one-dimensional (1D) subsonic carbon deflagration in a Chandrasekhar mass (M_{ch}) C–O white dwarf (Nomoto et al. 1984) produces sufficient amount of ^{56}Ni ($0.5 - 0.6 M_{\odot}$) and IMEs to explain a range of normal SNe Ia. However, studies show that the deflagration turns into a supersonic detonation at a transition density (Khokhlov et al. 1993; Hoefflich et al. 1995; Hoefflich & Khokhlov 1996; Höflich et al. 2002; Seitenzahl et al. 2013; Sim et al. 2013). By varying the transition density, a wide range of ^{56}Ni mass can be produced. These are called deflagration-to-detonation transition (DDT). These models can reproduce the observed luminosity in normal and subluminescent Ia and also the abundance stratification (Stehle et al. 2005) of the elements in the ejecta. Another variation of the standard detonation is the pulsational-delayed detonation (Hoefflich et al. 1995; Hoefflich & Khokhlov 1996; Dessart et al. 2014), in which deflagration causes expansion of the white dwarf followed by the infall of the expanding matter and hence compression of the white dwarf. This compression leads to a detonation at some particular density. It allows for more unburnt material in the ejecta. The widely favored model is the M_{ch} explosion of C–O white dwarf (Han & Podsiadlowski 2004). However, sub-Chandrasekhar mass detonation models can also reproduce a range of the observed properties of SNe Ia (Kromer et al. 2010; Sim et al. 2012; Shen et al. 2018).

For SNe Iax, the lower line velocities suggest that the explosion energies must be lower. The explosion produces less amount of ejecta as compared to SNe Ia and leaves behind a bound remnant (Kawabata et al. 2021). The abundance distribution in the ejecta is mixed (Li et al. 2003; Branch et al. 2004). These features can be explained by pure deflagration of M_{ch} C–O white dwarf of varying strengths (Kromer et al. 2013; Fink et al. 2014). These models can produce a range of ^{56}Ni mass and hence the luminosity observed in bright and intermediate

Table 1
Parameters of SN 2020csk and its Host Galaxy

Parameters	Value	Ref.
<i>SN 2020csk/ZTF20abwrcmq:</i>		
R.A. (J2000)	$\alpha = 01^{\text{h}}10^{\text{m}}34^{\text{s}}.84$	2
Decl. (J2000)	$\delta = +02^{\circ}06'50''.15$	2
Discovery Date	2020 August 25 10:03 UT (JD 2,459,086.92)	2
Last non-detection	2020 August 25 09:07 UT (JD 2,459,086.88)	2
Date of explosion	2020-08-20 21:15 UT $2, 459, 082.39^{+1.57}_{-1.37}$	1
Date of <i>B</i> -band Maxima	2020 September 06 08:09 UT (JD 2,459,098.84 \pm 0.30)	1
$\Delta m_{15}(B)$	2.03 ± 0.05 mag	1
Galaxy reddening	$E(B - V) = 0.0256 \pm 0.0014$ mag	3
Host reddening	$E(B - V) = 0.00$ mag	1
^{56}Ni mass	$M_{\text{Ni}} = 0.13^{+0.02}_{-0.01} M_{\odot}$	1
Ejected mass	$M_{\text{ej}} = 0.34^{+0.07}_{-0.10} M_{\odot}$	1
Kinetic energy	$E_{\text{K}} = 0.05^{+0.01}_{-0.01} \times 10^{51}$ erg s^{-1}	1
<i>Host galaxy:</i>		
Name	2MASX J01103497+0206508	
Type	H-II galaxy	4
RA (J2000)	$\alpha = 01^{\text{h}}10^{\text{m}}34^{\text{s}}.99$	4
DEC (J2000)	$\delta = +02^{\circ}06'51''.48$	4
Redshift	$z = 0.016 \pm 0.00010$	4
Distance modulus	$\mu = 34.24 \pm 0.22$ mag	5
$12 + \log(\frac{O}{H})$	8.54 ± 0.05 dex	1
SFR	$0.09 M_{\odot} \text{ yr}^{-1}$	1

Note. (1) This paper; (2) Fremling (2020); Prentice et al. (2020); (3) Schlafly & Finkbeiner (2011); (4) Skrutskie et al. (2006); (5) <http://leda.univ-lyon1.fr/>.

luminosity SNe Iax. For the fainter SNe Iax, like SN 2008ha, pure deflagration in M_{ch} carbon-oxygen-neon (C–O–Ne) white dwarfs has been proposed (Kromer et al. 2015).

SNe Iax show signatures of unburned carbon/oxygen in their spectra. These are essential in understanding the explosion models. Three-dimensional deflagration will produce unburned material in the inner parts of the ejecta near the center. A detonation will burn the materials in the inner regions and leave unburned material at lower density outer regions (Gamezo et al. 2003). The velocity of the unburned layers can constrain the models. The presence of C–O indicates the nature of the progenitor—carbon-oxygen (C–O) white dwarfs (Phillips et al. 2007) or carbon-oxygen-neon white dwarfs (Kromer et al. 2015) for the lower luminous subclass of SNe Iax.

The observed diversity and the possibility of a diverse class of progenitors make it important to study SNe Iax. The study of a recent SN Iax, SN 2020csk is presented in this work. SN 2020csk was discovered by Fremling (2020) on 2020 August 25, 10:03 UT (JD = 2,459,086.92) with a magnitude of 19.7 mag in ZTF-*r* filter. The last non-detection was reported on 2020 August 25 09:07 UT with a limiting magnitude of 20.63 mag in the same filter. The object was classified as a SN Iax by Prentice et al. (2020) based on a spectrum obtained on 2020 August 30, 03:43 UT (JD = 2459091.66) by the Liverpool Telescope. The important parameters of SN 2020csk and its host galaxy are presented in Table 1.

The details of the observations are presented in Section 2. Section 3 and Section 4 present the analysis of light curve and

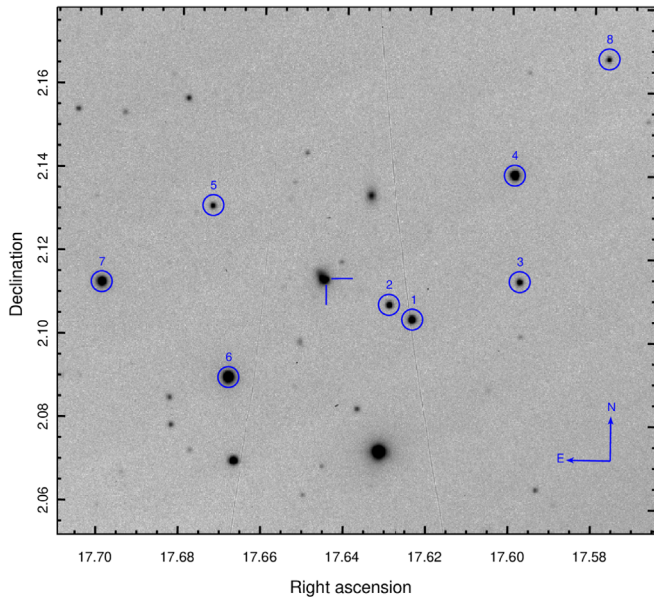


Figure 1. The field of SN 2020sck. This is a $\sim 7 \times 7$ arcmin² image in *B*-band (300 s exposure) taken with HCT on 2020 September 11. The stars circled in blue are the secondary standards used for calibration purpose. The SN is marked with crosshairs.

spectral evolution. Spectral modeling of SN 2020sck with SYN++ and TARDIS is presented in Section 5. In Section 6 we discuss the host galaxy and its properties. Possible explosion models are discussed in Section 7. Finally, we summarize our results in Section 8.

2. Observations and Data Reductions

2.1. Optical Photometry

Imaging of SN 2020sck in Bessell’s *UBVRI* bands was carried out with the Himalayan Faint Object Spectrograph Camera (HFOSC) mounted on the 2.0 m Himalayan Chandra Telescope located at the Indian Astronomical Observatory (IAO) at Hanle, India⁸ (Figure 1). Photometric observations with HCT started on 2020 August 31, at 5.4 days before *B*-band maximum and continued until 2020 November 13. A set of local standard stars in the SN field was calibrated using Landolt standards PG 1633+099 and PG 0231+051 observed on 2020 September 01, PG 2331+055 and PG 2213-006 observed on 2020 September 07, PG 2331+055 observed on 2020 September 24, PG 0231+051 observed on 20 September 27 and PG 2213-006 observed on 2020 October 25. The *UBVRI* magnitudes of the local standard stars are listed in Table 8. To obtain the SN magnitudes, template subtraction has been performed. Deep stacked images of the SN field was observed on 2021 July 16 under good seeing conditions after the SN has faded beyond the detection limit. Details of the data reduction can be found in Dutta et al. (2021).

SN 2020sck was followed up in SDSS-*r'*-filter with the 0.7 m fully robotic GROWTH-India Telescope (GIT)⁹ at IAO, equipped with a 2148×1472 pixels Apogee Camera. The

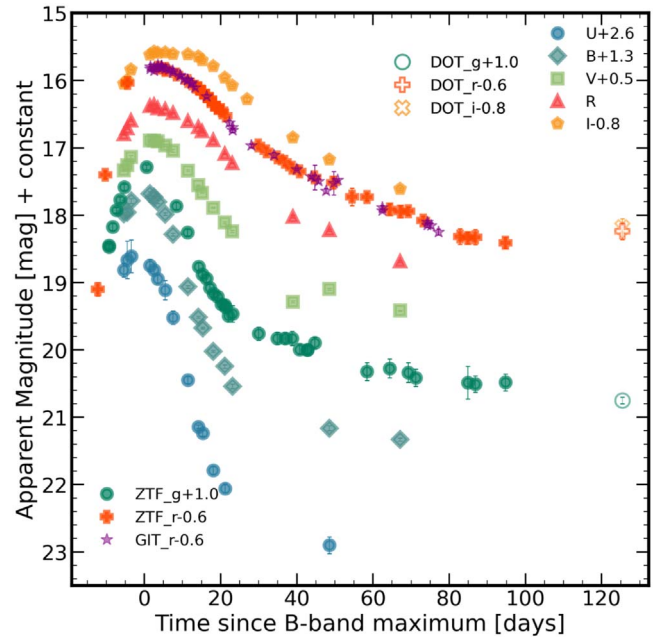


Figure 2. *UBVRI*, ZTF-*g*, ZTF-*r*, and GIT-*r'*-band light curves of SN 2020sck. Also plotted are the *g*, *r*, and *i*-band magnitudes obtained from DOT. The phase is measured with respect to the *B*-band maximum. The light curves in individual bands have been shifted for representation purpose. The *UBVRI* band magnitudes are in the *Vega* system, while the ZTF-*g*, ZTF-*r*, GIT-*r'*, DOT-*g*, DOT-*r*, and DOT-*i*-band magnitudes are in the *AB* system. The HCT, GIT, and DOT photometric data are available as data behind the Figure.

(The data used to create this figure are available.)

observations began on 2020 September 07 and continued until 2020 November 23. GIT can be used in both targeted and tiled modes of operation. We used the targeted mode of operation and obtained 300 s exposure images. PanSTARRS image of the field in *r*-filter was used as the reference image for host galaxy subtraction and the photometric zero-points were calculated using the PanSTARRS catalog (Flewelling 2018). We used PYZOGY, which is based on ZOGY algorithm (Zackay et al. 2016) to perform the image subtraction. Finally, the PSF model generated by PSFex (Bertin 2011) for the GIT image was used for photometry of the SN. The SN magnitudes in Bessell *UBVRI* and SDSS-*r'* are available as data behind Figure 2.

Late phase observations of SN 2020sck was carried out with the ARIES-Devasthal Faint Object Spectrograph and Camera mounted on the axial port of the 3.6 m Devasthal Optical Telescope (DOT; Omar et al. 2019). Imaging in SDSS-*g*, *r*, and *i* bands was performed on 2021 January 11. The data has been reduced in the standard manner as for HFOSC. To obtain the SN magnitudes, template subtraction has been performed with SDSS images in *g*, *r*, and *i* bands. The SN magnitudes were calibrated using photometric zero-points calculated using the SDSS catalog (Ahumada et al. 2020). The magnitudes obtained with DOT are available as data behind Figure 2.

SN 2020sck was also observed with the Zwicky Transient Facility (ZTF, Bellm et al. 2019). The photometric data in *g* and *r* bands was collected from the public archive.¹⁰

⁸ https://www.iap.res.in/?q=telescope_iao

⁹ Global Relay of Observatories Watching Transients Happen (<https://www.growth.caltech.edu/>), (<https://sites.google.com/view/growthindia/>).

¹⁰ <https://alerce.online/>

Table 2
Photometric Parameters of SN 2020sck

Filter	$\lambda_{\text{eff}}(\text{\AA})$	JD (Max)	m_{λ}^{max}	$\Delta m_{15}(\lambda)$	M_{λ}^{max}	Colors at B max
U	3663.6	$2,459,096.84 \pm 0.57$	16.03 ± 0.06	2.17 ± 0.06	-18.33 ± 0.23	...
B	4363.2	$2,459,098.84 \pm 0.30$	16.53 ± 0.02	2.03 ± 0.05	-17.81 ± 0.22	$(U - B)_0 = -0.35 \pm 0.02$
V	5445.8	$2,459,100.84 \pm 0.26$	16.41 ± 0.02	0.80 ± 0.03	-17.91 ± 0.22	$(B - V)_0 = -0.08 \pm 0.03$
R	6414.2	$2,459,101.57 \pm 0.48$	16.39 ± 0.01	0.42 ± 0.02	-17.93 ± 0.22	$(V - R)_0 = -0.01 \pm 0.01$
I	7978.8	$2,459,103.58 \pm 1.40$	16.37 ± 0.02	0.27 ± 0.02	-17.91 ± 0.22	$(R - I)_0 = -0.02 \pm 0.01$
$ZTF - g$	4722.7	$2,459,099.14 \pm 0.34$	16.27 ± 0.03	1.54 ± 0.04	-18.07 ± 0.22	...
$ZTF - r$	6339.6	$2,459,100.28 \pm 0.76$	16.34 ± 0.03	0.49 ± 0.03	-17.96 ± 0.22	...

2.2. Optical Spectroscopy

Spectroscopic monitoring of SN 2020sck with HCT started on 2020 October 31 (JD = 2459093.31) and continued until 2020 October 03 (JD = 2459126.34). Low–medium-resolution spectra were obtained using grisms Gr7 (3500–7800 Å) and Gr8 (5200–9100 Å) available with HFOC. The log of spectroscopic observations is provided in Table 9. The spectra have been corrected for a redshift of $z = 0.016$. Telluric features have been removed from the spectra. The data reduction was performed using the procedure described in Dutta et al. 2021.

2.3. Extinction and Distance Modulus

The reddening due to the SN host galaxy for SNe Ia can be estimated from the $(B - V)$ color evolution of the SN during 30–90 days since the B -band maximum (Phillips et al. 1999). However, this relation may not strictly hold for SNe Iax, due to the scatter in the evolution (Foley et al. 2013). The reddening within the host galaxy can also be estimated by the detection of interstellar Na I D line (Turatto et al. 2003; Poznanski et al. 2012). We do not detect the Na I D line in our low-resolution spectra. Therefore, assuming zero host galaxy extinction, we correct the data only for the Galactic reddening of $E(B - V) = 0.0256$ (Schlafly & Finkbeiner 2011) with $R_V = 3.1$ (Fitzpatrick 1999). From the prominent hydrogen emission lines in the spectra of SN 2020sck, we estimate a redshift of $z = 0.016$ for the host galaxy. Using a distance modulus of $\mu = 34.24 \pm 0.22$ mag¹¹ derived from the Virgo infall assuming $H_0 = 70 \text{ km s}^{-1} \text{ Mpc}^{-1}$ (Makarov et al. 2014), we find the absolute magnitude M_B to be -17.81 ± 0.22 mag.

3. Light Curve

3.1. Light Curve Analysis

The light curves of SN 2020sck in the U , B , g , V , r , R , and I bands are shown in Figure 2. SN 2020sck was followed from -5.38 days to $+67.11$ days since the B -band maximum in $UBVRI$ bands and -13.36 days to $+95.42$ days since the r -band maximum in $ZTF-g$ and $ZTF-r$ bands. We fit the $UBVRI$, $ZTF-g$, and $ZTF-r$ bands with Gaussian process regression (Rasmussen & Williams 2006) using the `Gaussian_process` package in `scikit-learn` (Pedregosa et al. 2011) and find the epoch of maximum magnitude and the associated errors in each band. Table 2 lists the important photometric parameters of SN 2020sck. SN 2020sck reached its peak B -band magnitude of 16.53 ± 0.02 mag at JD 2,459,098.84. The maximum in U -band occurred at -2.0 days and that in V , R , and I bands at $+2$ days, $+2.8$, and $+4.7$ days, respectively

since the B -band maximum. This indicates that the ejecta is cooling with time and follows a simple thermal model. The delay in V -band with respect to the B -band maximum is similar to that seen in SN 2002cx and SN 2005hk. The R and I bands show no secondary maximum as are seen for SNe Ia. In Figure 3 the light curves of SN 2020sck in $UBVRI$ have been compared with other SNe Iax. SN 2020sck has a decline rate of $\Delta m_{15}(B) = 2.03 \pm 0.05$ mag in B -band, which is faster than bright SNe Iax like SN 2002cx and SN 2005hk and slower than some of the low luminosity objects like SN 2008ha, SN 2010ae, SN 2019muj. SN 2020sck shows a decline rate in V -band ($\Delta m_{15}(V) = 0.80$ mag) similar to SN 2002cx and SN 2012Z. The redder bands show slower decline ($\Delta m_{15}(R) = 0.42$ mag, $\Delta m_{15}(I) = 0.27$ mag).

Figure 4 shows the comparison of $ZTF-g$ and $ZTF-r$ band light curves of SN 2020sck along with other SNe Iax in similar filters. The decline rate in g -band ($\Delta m_{15}(g) = 1.54$ mag) is similar to SN 2010ae and SN 2014ck. SN 2020sck has the slowest decline in r -band with a $m_{15}(r) = 0.49 \pm 0.03$ mag. The decline rate for SN 2005hk and SN 2012Z in r -band are 0.70 mag and 0.66 mag respectively. For the fainter SNe Iax, the decline rate in r band is faster. Table 3 provides the observed properties of the other SNe Iax used for comparison.

The light curve decline rate of SN 2020sck is similar to the lower luminosity SNe Iax in the blue bands, while it is similar to the brighter objects in the red bands. The $(U - B)$, $(B - V)$, $(V - R)$, $(R - I)$, and $(g - r)$ color evolutions of SN 2020sck are plotted in Figures 5 and 6 and compared with other SNe Iax. The overall trend of the color evolution of SN 2020sck is similar to other well-studied SN Iax events. The $(U - B)$ color evolution is similar to SN 2005hk and SN 2011ay. The $(B - V)$ color is bluer near maximum in B -band (-0.08 ± 0.03 mag) and follows the same trend as other SNe Iax in the later phase. In comparison, the $(B - V)$ color at B -max is 0.04 mag for SN 2002cx and -0.03 mag for SN 2005hk. The $(V - R)$ color is also bluer than the comparison SNe. The $(R - I)$ and $(g - r)$ color evolution is similar to SN 2005hk.

3.2. Estimation of Time of First Light

During the early times of the explosion, the luminosity is proportional to the surface area of an expanding fireball and hence increases as t^2 , where t is the time since the explosion. This assumes that the photospheric velocity and temperature do not change significantly during this phase (Riess et al. 1999). SN 2020sck was monitored with ZTF soon after its discovery (\sim JD 2,459,086) in g and r bands. This allows us to place a constraint on the time of first light. We fit the early g -band data of ZTF with a power law of the form

$$F(t) = A(t - t_0)^n, \quad (1)$$

¹¹ <http://leda.univ-lyon1.fr/>

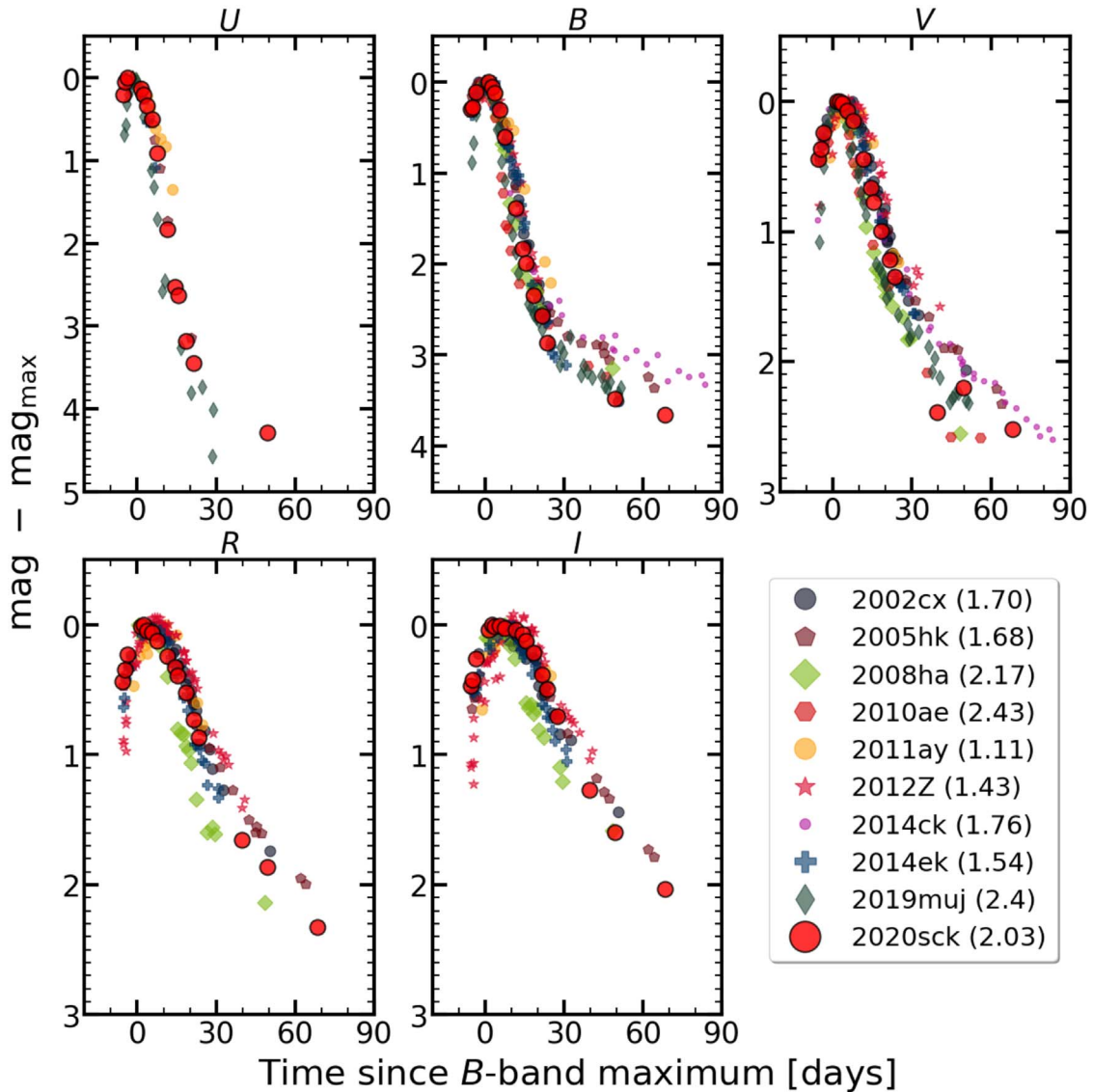


Figure 3. *UBVR-I*-band light curves of SN 2020sck plotted along with other SNe Iax. The phase is measured with respect to the *B*-band maximum. The light curves have been shifted to match with their respective peak magnitudes. The $\Delta m_{15}(B)$ of each SN are quoted in parentheses.

where A is a normalization constant, t_0 is the time of first light and n is the power-law index. For the “fireball model” the value of n is 2. The variation from this value hints toward the distribution of ^{56}Ni in the ejecta, with a lower index pointing toward higher degrees of mixing (Firth et al. 2015). The value of n varies from ~ 1.5 to ~ 3.5 . In the fit, we kept n as a free parameter. We aimed to fit the *g*-band flux with a starting value of $t_0 = 2,459,086$ from the non-detection. However, from the fit, we get an unrealistic value of $n = 0.39$. Next, we kept the starting value of t_0 between 2,459,080 and 2,459,087 and from the fit we obtain an explosion date of 2020 August 20 21:15 UT (JD = $2,459,082.39^{+1.37}_{-1.37}$) and an exponent(n) of $1.79^{+0.29}_{-0.33}$. We use JD 2,459,082.4 as the explosion date throughout the work. The power-law fit is shown in Figure 7. From the fit, we estimate the rise time to the maximum in *g*-band as 16.75 days and in *r*-band as 17.89 days. The rise time for SN 2020sck is similar to SN 2002cx-like objects, for which the rise time is ~ 15.0 days. The rise times for SN 2005hk (Phillips et al. 2007) and SN 2015H (Magee et al. 2016) are 15.0 days and 15.9 days

(*r*-band) respectively. While SN 2008ha (Foley et al. 2009), SN 2012Z (Yamanaka et al. 2015), and SN 2019muj (Barna et al. 2021) have lower rise times of 10, 12.0, and 9.6 days respectively, the rise time for SN 2009ku (Narayan et al. 2011) is 18.2 days, close to that for SNe Ia (~ 19.0 days).

3.3. Estimation of Nickel Mass

The bolometric light curve has been calculated using the *U*, *B*, *V*, *R*, and *I*-band magnitudes. The apparent magnitudes were corrected for the Milky Way reddening of $E(B - V) = 0.0256$ and $R_V = 3.1$. The reddening corrected magnitudes were converted into flux units using zero-points from Bessell et al. (1998). A third-order spline curve was fit to the spectral energy distribution (SED) and the area under the curve was calculated using trapezoidal rule integrating from 3000 to 9500 Å. For SNe Iax, due to the scatter in the light curve evolution, a well-defined correction factor in UV and IR does not exist. However, some SNe have been possible to observe in UV to IR wavelength range. For SN 2005hk, Phillips et al. (2007)

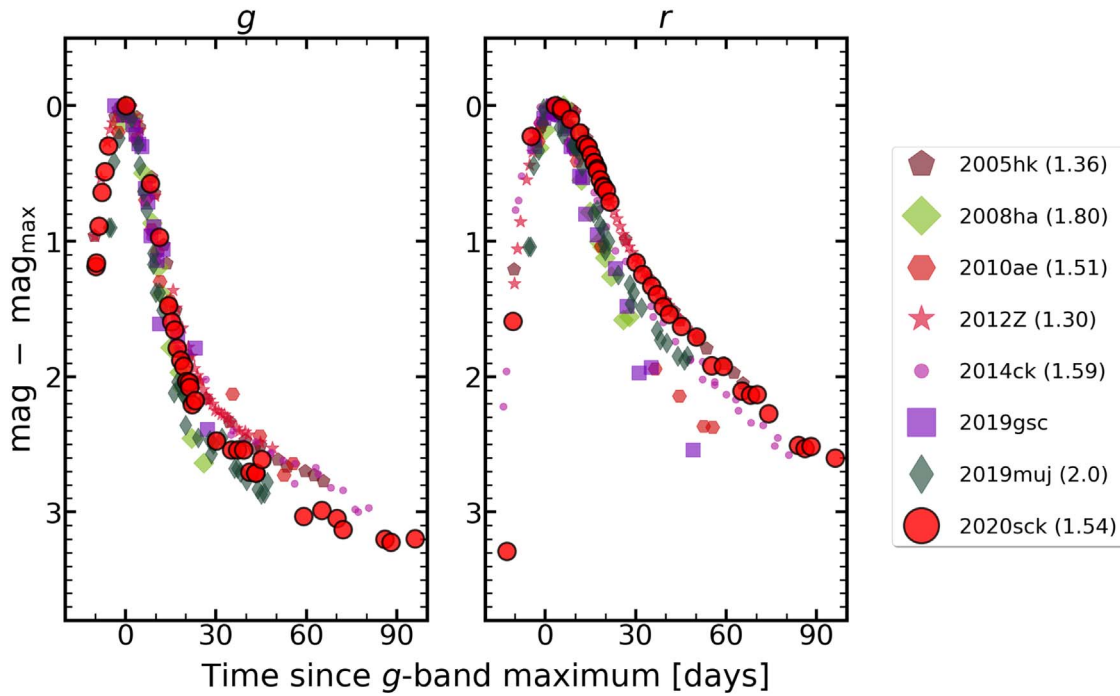


Figure 4. ZTF-*g* and ZTF-*r* light curves of SN 2020sck plotted along with other SNe Iax in similar filters. The phase is measured with respect to the *g*-band maximum. The light curves have been shifted to match with their respective peak magnitudes. The $\Delta m_{15}(g)$ of each SN are quoted in parentheses. The light curve data for SN 2020sck has been obtained from <https://alerce.online/object/ZTF20abwrcmq>.

Table 3
Properties of the Comparison Sample

SN (Name)	M_B (mag)	M_V (mag)	$\Delta m_{15}(B)$ (mag)	$\Delta m_{15}(V)$ (mag)	$\Delta m_{15}(g)$ (mag)	$\Delta m_{15}(r)$ (mag)	$12 + \log\left(\frac{O}{H}\right)$ (dex)	Reference
SN 2002cx	-17.53 ± 0.26	-17.49 ± 0.22	1.70 ± 0.1	0.73	1, 2
SN 2005hk	-18.02 ± 0.32	-18.08 ± 0.29	1.68 ± 0.05	0.92	1.36 ± 0.01	0.70	...	2, 3
SN 2008 ha	-13.74 ± 0.15	-14.21 ± 0.15	2.17 ± 0.02	1.29	1.80 ± 0.03	1.11	8.16 ± 0.15	4
SN 2009ku	-18.4	...	0.59	5
SN 2010ae	-13.44 ± 0.54	-13.80	2.43 ± 0.11	1.15	1.51 ± 0.05	1.01	8.40 ± 0.18	6
SN 2011ay	-18.15 ± 0.17	-18.39 ± 0.18	1.11 ± 0.16	0.95	7
SN 2012Z	-17.61	-18.04	1.57 ± 0.07	0.89	1.30 ± 0.01	0.66	8.51 ± 0.31	8
PS1-12bwh	1.35 ± 0.09	0.60	8.87 ± 0.19	9
SN 2013en	10
SN 2014ck	-17.37 ± 0.15	-17.29 ± 0.15	1.76 ± 0.15	0.88	1.59 ± 0.1	0.58	...	11
SN 2014dt	-18.13 ± 0.04	-18.33 ± 0.02	1.35 ± 0.06	12
SN 2014ek	-17.32 ± 0.23	-17.66 ± 0.20	1.54 ± 0.17	0.90	13
SN 2015H	0.69	...	14
SN 2019gsc	0.91	8.10 ± 0.06	15
SN 2019muj	-16.36 ± 0.06	-16.42 ± 0.0	2.4	1.2	2.0	1.0	...	16

References: (1) Li et al. (2003); (2) Phillips et al. (2007); (3) Sahu et al. (2008); (4) Foley et al. (2009); (5) Narayan et al. (2011); (6) Stritzinger et al. (2014); (7) Szalai et al. (2015); (8) Yamanaka et al. (2015); (9) Magee et al. (2017); (10) Liu et al. (2015); (11) Tomasella et al. (2016); (12) Singh et al. (2018); (13) Li et al. (2018); (14) Magee et al. (2016); (15) Srivastav et al. (2020); (16) Barna et al. (2021).

have ignored the NIR flux contribution to the UVOIR bolometric light curve during the early phase and have used about $\sim 20\%$ contribution to the flux in UV before maximum. For SN 2012Z, Yamanaka et al. (2015) have shown that the ratio of the flux in IR to the combined flux in optical and IR increases from 0.15 to 0.3 from around 8–25 days since the explosion. However, the evolution is significantly different from that found in SN Ia. For SN 2014ck, Tomasella et al. (2016) have assumed a 10% contribution to the UV flux at maximum. SN 2014dt showed a significant increase in NIR and mid-IR flux from about 100 days post-maximum in *B*-band

(Fox et al. 2016). For SN 2019gsc, Tomasella et al. (2020) found that the peak *gri* bolometric luminosity is 53% of the peak OIR bolometric luminosity. To find the missing flux in UV and IR, a blackbody fit to the SED has been performed and added to the optical flux. This approach does not take into account the line-blanketing effects in the UV range and assumes that there is a contribution of UV and IR flux throughout the evolution of the bolometric light curve. The total flux thus obtained has been converted to luminosity assuming a distance modulus of $\mu = 34.24$ mag. The quasi-bolometric light curve is shown in Figure 8. We model the

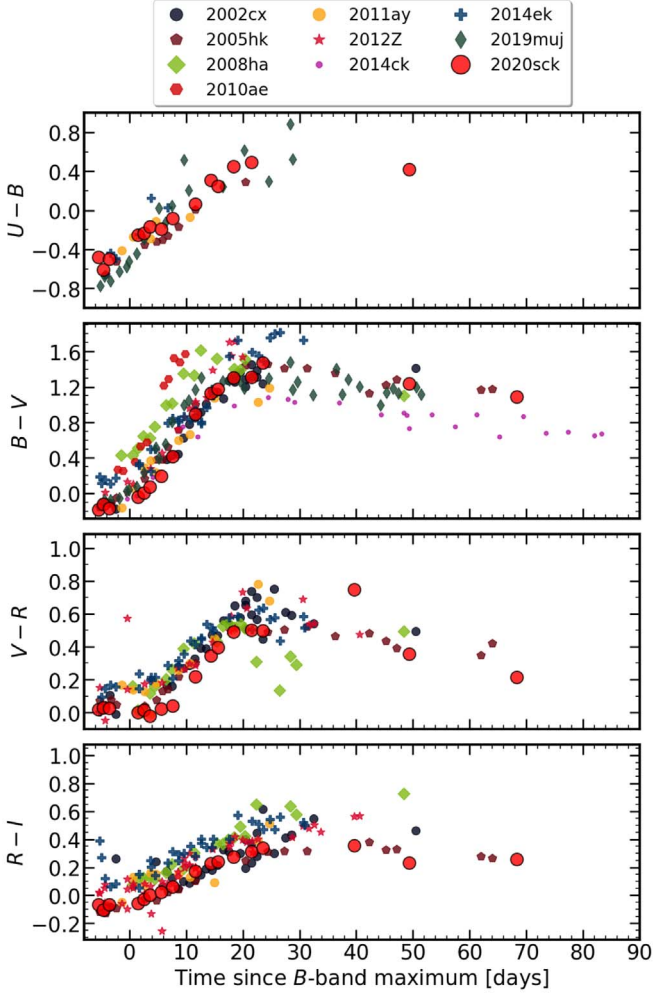


Figure 5. $(U - B)$, $(B - V)$, $(V - R)$ and $(R - I)$ color evolution of SN 2020sck plotted with other SNe Iax.

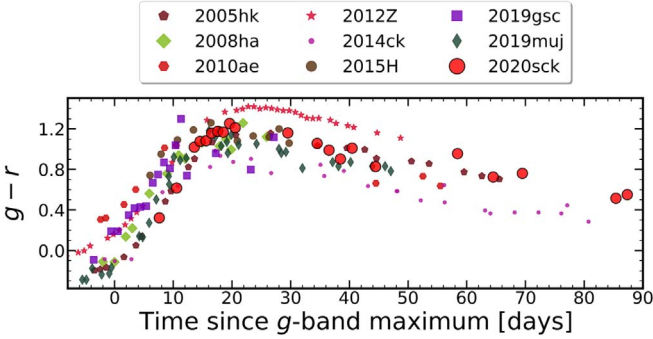


Figure 6. $(g - r)$ color evolution of SN 2020sck plotted along with other SNe Iax.

quasi-bolometric light curve as Gaussian process using the `Gaussian_process` package in `Scikit-learn` and estimate the peak luminosity for SN 2020sck to be $L_{\text{peak}}^{\text{quasi-bol}} = (3.41 \pm 0.25) \times 10^{42} \text{ erg s}^{-1}$. The peak luminosity for the blackbody bolometric light curve is $L_{\text{peak}}^{\text{BB}} = (5.51 \pm 0.54) \times 10^{42} \text{ erg s}^{-1}$. The peak quasi-bolometric luminosity is 62% of the peak blackbody bolometric luminosity ($L_{\text{opt}}/L_{\text{BB}}$). For SN 2019gsc, $L_{\text{opt}}/L_{\text{BB}}$ is 69 % using a similar approach (Srivastav et al. 2020).

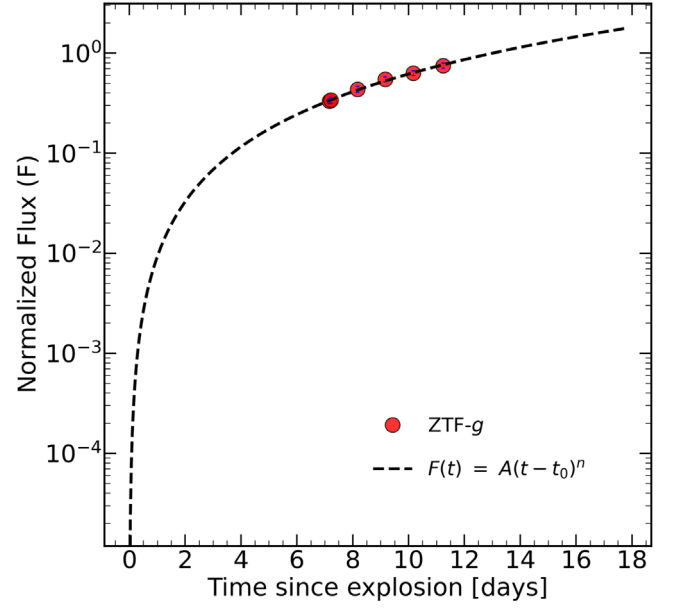


Figure 7. $F \sim t^n$ fit to the pre-maximum ZTF-g band light curve. Flux error is shown in blue.

To estimate the amount of nickel synthesized in the explosion, we fit the bolometric light curves with a modified radiation diffusion model (Arnett 1982; Valenti et al. 2008; Chatzopoulos et al. 2012). The modified model takes into account the diffusion of radioactive decay energy from ^{56}Ni and ^{56}Co and also the gamma-ray leakage from the ejecta. The output luminosity is expressed as:

$$L(t) = M_{\text{Ni}} e^{-x^2} [(\epsilon_{\text{Ni}} - \epsilon_{\text{Co}}) \int_0^x 2z e^{z^2 - 2zy} dz + \epsilon_{\text{Co}} \int_0^x 2z e^{z^2 - 2yz + 2zs} dz] (1 - e^{-(\frac{t}{\tau})^2}), \quad (2)$$

where $x \equiv t/t_{\text{lc}}$, t is the time since explosion (days) and t_{lc} is the light curve timescale (days). $y \equiv t_{\text{lc}}/(2t_{\text{Ni}})$ with $t_{\text{Ni}} = 8.8$ days, $s \equiv [t_{\text{lc}}(t_{\text{Co}} - t_{\text{Ni}})]/(2t_{\text{Co}}t_{\text{Ni}})$ with $t_{\text{Co}} = 111.3$ days. M_{Ni} is the initial Ni mass and t_{γ} is the gamma-ray timescale (days). Large t_{γ} means all the gamma rays and positrons are trapped. $\epsilon_{\text{Ni}} = 3.9 \times 10^{10} \text{ erg s}^{-1} \text{ g}^{-1}$ and $\epsilon_{\text{Co}} = 6.8 \times 10^9 \text{ erg s}^{-1} \text{ g}^{-1}$ are the energy generation rates due to the decay of Ni and Co respectively. The fit parameters of the model are t_{exp} —the epoch of explosion, M_{Ni} —the initial ^{56}Ni mass produced, t_{lc} —the light curve timescale and t_{γ} —the gamma-ray leaking timescale. We can obtain the ejecta mass (M_{ej}) and kinetic energy (E_{K}) using the relations:

$$M_{\text{ej}} = 0.5 \frac{\beta c}{\kappa} v_{\text{exp}} t_{\text{lc}}^2, \quad (3)$$

$$E_{\text{K}} = 0.3 M_{\text{ej}} v_{\text{exp}}^2. \quad (4)$$

Here, $\beta = 13.8$ is a constant of integration. c is the speed of light. v_{exp} is the expansion velocity of the ejecta.

To fit the model and find the model parameters that best describe our quasi-bolometric light curve, we sampled the posterior distribution and maximized the posterior by maximizing the product of the likelihood and the prior. The likelihood

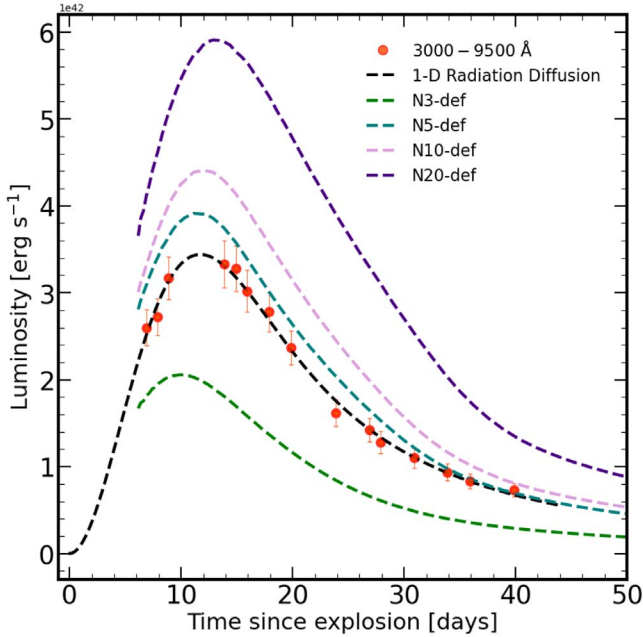


Figure 8. The quasi-bolometric light curve of SN 2020sck fitted with 1D radiation diffusion model. Also plotted are the angle-averaged bolometric light curve from the three-dimensional pure deflagration models of M_{ch} WD (Fink et al. 2014). The models have been obtained from the Heidelberg Supernova Model Archive (HESMA).

function is

$$\text{Log likelihood} = -\frac{1}{2} \sum_i \left(\frac{y_{\text{model}} - y_i}{y_{\text{err}}} \right)^2. \quad (5)$$

Here, y_{model} and y_i are the model luminosity and the measured luminosity respectively. y_{err} is the error in the measured luminosity. The sum runs over all the data points. We used flat or uniform prior for the model parameters— $0 < M_{\text{Ni}} < 1.4 M_{\odot}$, $t_{\text{lc}} > 0$ days, $t_{\gamma} > 0$ days, and $2,459,082 < t_{\text{exp}} < 2,459,090$. We used the `emcee` package in `python` to find the posterior distribution of the model parameters (Foreman-Mackey et al. 2013). Figure 9 shows the one- and two-dimensional projections of the posterior distribution of the fit parameters.

The fit to the quasi-bolometric light curve gives $t_{\text{exp}} = 2,459,084.96^{+1.58}_{-1.74}$, $M_{\text{Ni}} = 0.13^{+0.02}_{-0.01} M_{\odot}$, $t_{\text{lc}} = 10.75^{+2.47}_{-1.96}$ days, and $t_{\gamma} = 35.02^{+2.47}_{-3.00}$ days. Using a constant optical opacity $\kappa_{\text{opt}} = 0.1 \text{ cm}^2 \text{ g}^{-1}$ for a Fe dominated ejecta (Pinto & Eastman 2000; Szalai et al. 2015; Srivastav et al. 2020) and an expansion velocity $v_{\text{exp}} = 5000 \text{ km s}^{-1}$ derived from the SYN++ fitting of the near maximum spectrum, we get $M_{\text{ej}} = 0.34^{+0.07}_{-0.10} M_{\odot}$ and a kinetic energy of explosion $E_{\text{kinetic}} = 0.05^{+0.01}_{-0.01} \times 10^{51} \text{ erg}$. If we assume explosion of a M_{ch} white dwarf, the bound remnant mass is $1.06 M_{\odot}$. The fit to the blackbody bolometric light curve gives $M_{\text{Ni}} = 0.17^{+0.01}_{-0.01} M_{\odot}$.

The quasi-bolometric light curve of SN 2020sck has been compared with angle-averaged bolometric light curve from three-dimensional pure deflagrations of M_{ch} carbon-oxygen white dwarfs. In these models, no delayed detonations occur to completely unbind the white dwarf and thus a bound remnant is left behind (Fink et al. 2014). The explosion is parametrized by multiple spherical ignition spots that burn simultaneously. This allows exploring a wide range of explosion strengths. The models N1, N3, N5, N10, and N20 correspond to 1, 3, 5, 10, and 20 ignition spots, respectively, placed randomly around the

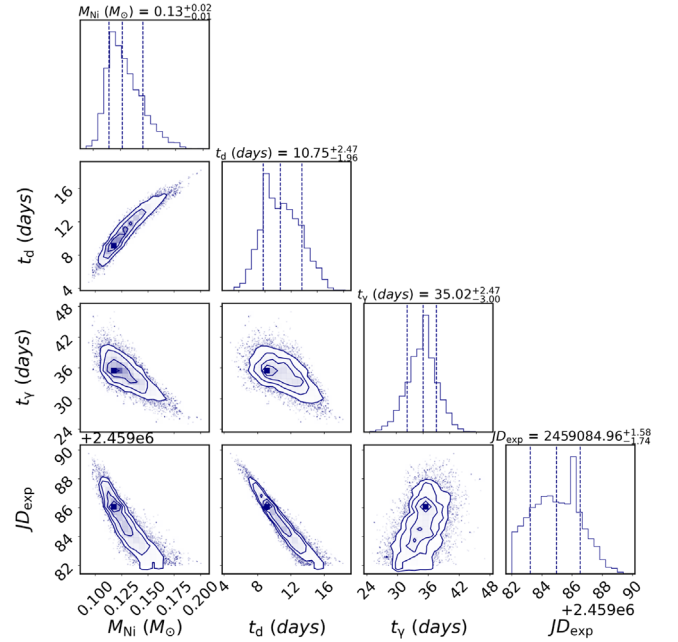


Figure 9. One- and two-dimensional projections of the posterior probability distribution of the fit parameters of Equation (2) to the quasi-bolometric light curve of SN 2020sck. The vertical dashed lines show the 16th, 50th and 84th percentiles of the samples in the distribution. See Figure 8 for the fit.

center of the white dwarf. The energy released in the explosion and the luminosity increases with an increasing number of spots. As the number of ignition spots increases, more matter is burnt and hence leads to higher expansion velocity of the ejecta. The model N5-def with $\Delta m_{15}(B) = 1.69$ mag and $M_B^{\text{max}} = -17.85$ mag matches closely with SN 2020sck, which has a $\Delta m_{15}(B) = 2.03$ mag and $M_B^{\text{max}} = -17.81$ mag. In the N5-def model, the mass of ^{56}Ni is $0.16 M_{\odot}$, the ejecta mass is $0.372 M_{\odot}$, the mass of the bound remnant is $1.03 M_{\odot}$. These values match closely with that estimated for SN 2020sck from the quasi-bolometric light curve fit with the radiation diffusion model. The kinetic energy estimated by the N5-def model is $0.135 \times 10^{51} \text{ erg}$, the radiation diffusion model gives an estimate of $0.05 \times 10^{51} \text{ erg}$. The models with lesser number of ignition points (1, 3, 5) evolve in an asymmetric way compared to models with larger number of ignition kernels (150, 300 etc). So, moderate viewing angle dependence is possible in these deflagration models (Fink et al. 2014). The lower kinetic energy estimated by the radiation diffusion model can be explained if we assume that the explosion is similar to N5-def but with a lower line-of-sight velocity.

4. Spectral Analysis

4.1. Spectral Evolution

The spectroscopic evolution of SN 2020sck is shown in Figure 10. The line identification has been done by comparing with SN 2002cx (Branch et al. 2004) and SN 2005hk (Sahu et al. 2008) around similar phases, and also with the spectrum synthesis code SYN++ (Thomas et al. 2011). The spectra in the pre-maximum phase show a blue continuum and presence of absorption features due to Fe III ($\lambda 4420, 5075, 5156$), Fe II ($\lambda 4924$), and Si III ($\lambda 4568$), a weak absorption feature of Co II ($\lambda 4161$) around $\sim 4000 \text{ \AA}$, Si II ($\lambda 5449, 5623$), and an asymmetric weak absorption feature at $\sim 6200 \text{ \AA}$ due to Si II

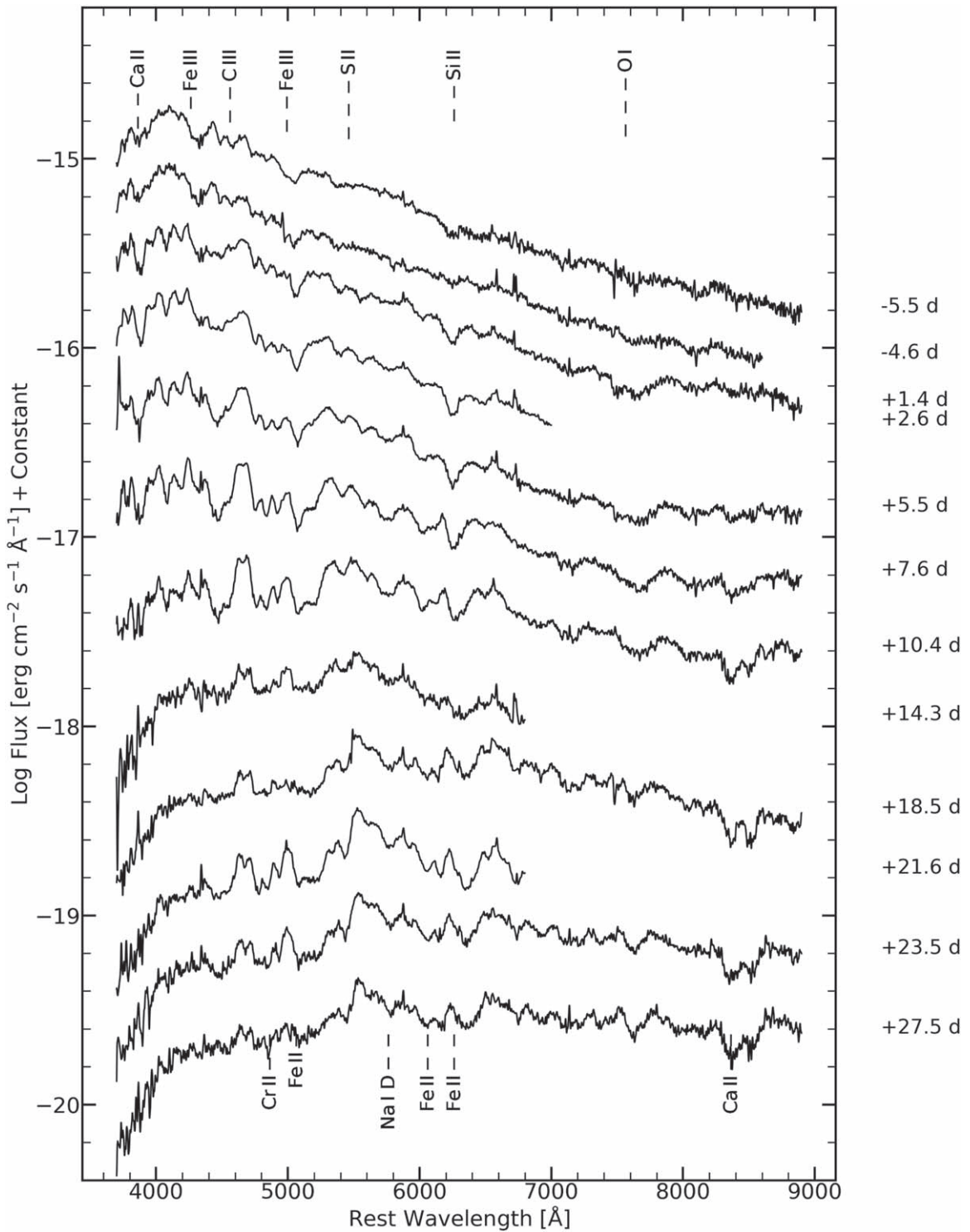


Figure 10. Spectral evolution of SN 2020sck from -5.5 to $+27.5$ day since the B -band maximum. The spectra are dereddened and redshift corrected. The telluric features have been removed. Spectra have been smoothed for visual clarity. A detailed spectral line identification is shown in Figure 11.

($\lambda 6355$). We compare the spectra of SN 2020sck in the pre-maximum phase with other SNe Iax in panel (a) of Figure 11. All the SNe except SN 2014ck show a blue continuum. The lines due to Fe III (~ 4420 Å) and Fe III (~ 5156 Å) are prominent in all the SNe with varying optical depth. The -5.4 days spectrum of SN 2020sck is similar to SN 2005hk and SN 2019muj. The weak IME features seen in SN 2020sck is possibly due to lower density and lesser optical depth in the

outer regions, which allows us to probe the hotter inner regions of the ejecta. The presence of higher ionization states of IMEs (Si III) and IGEs (Fe III) also indicates a hot photosphere. SN 2014ck shows deeper Si II ($\lambda 6355$) and S II features. This is because of the lower luminosity and lower photospheric temperature. Prominent C II ($\lambda 6580$) absorption feature is present in the spectrum of SN 2014ck and SN 2019muj in the pre-maximum phase. But for SN 2020sck, C II feature is not

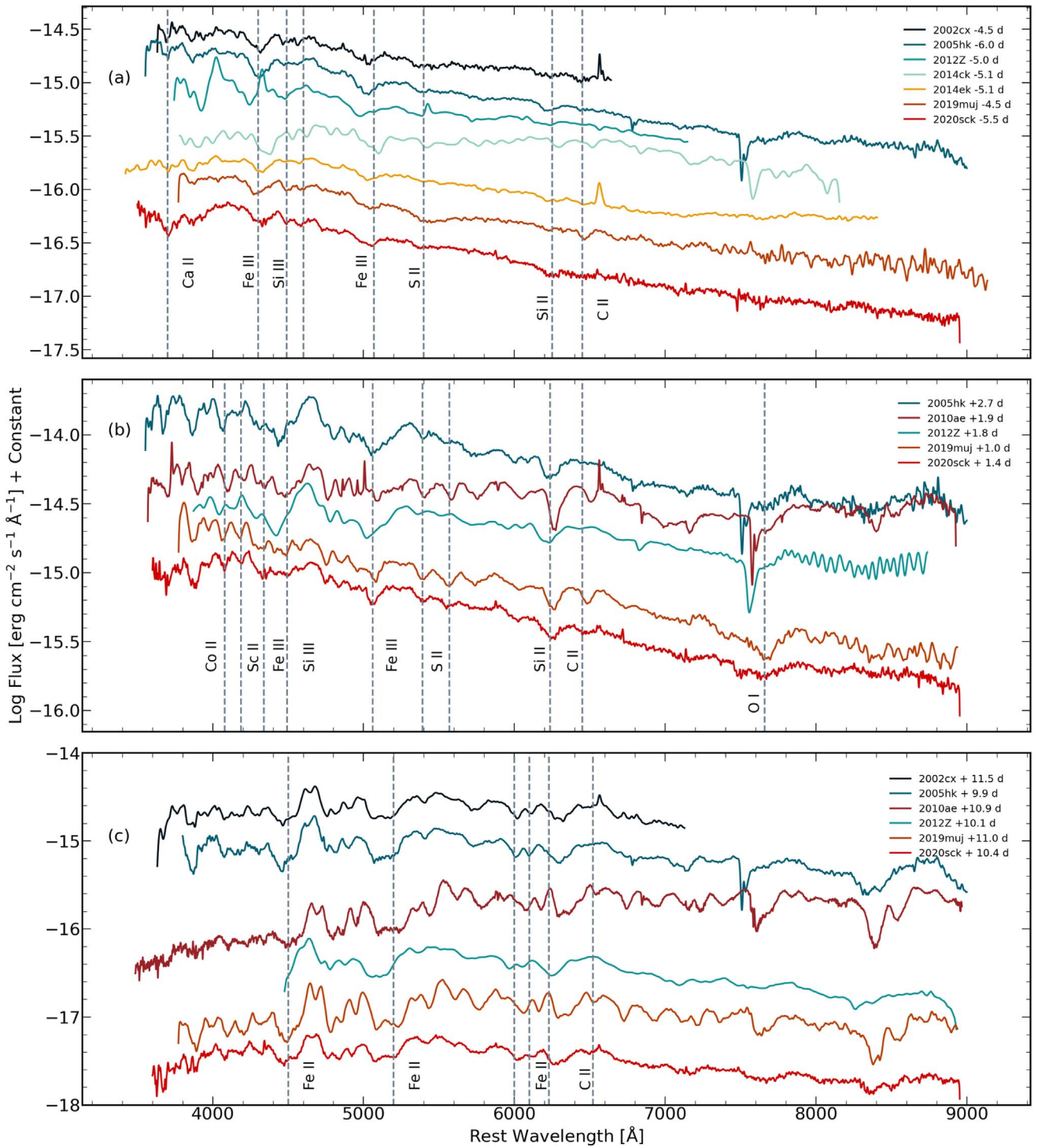


Figure 11. Comparison of the spectra of SN 2020sck with other SNe Iax around similar phase. The dashed vertical lines show the position of the absorption minima of the ions for SN 2020sck. All the spectra have been smoothed for visual clarity.

seen to be developed. This hints toward the fact that the outer layers of the ejecta has lesser C in SN 2020sck.

Around maximum the absorption features of Si II ($\lambda 6355$) and S II ($\lambda 5449, 5623$) become prominent. Ca II H & K ($\lambda\lambda 3934, 3968$) and Ca II NIR triplet ($\lambda 8498$) are seen to be developing. A O I ($\lambda 7775$) feature is prominently visible. C II ($\lambda 6580$) and C III ($\lambda 4647$) absorption features can be seen in the spectrum taken at +1.4 days. A C II ($\lambda 6580$) feature begins to appear around maximum with a pseudoequivalent width

(pEW) of $5.25 \pm 1.05 \text{ \AA}$ at +1.4 days. This feature is present in our spectrum until +10.4 days. Appearance of C in the near-maximum phase implies that the C layer is mixed in the ejecta. Comparing with other SNe Iax, it is seen that SN 2014ck and SN 2019muj also show prominent C II ($\lambda 6580$) feature with pEW of 4 \AA and 12 \AA respectively. In the near-maximum phase, the spectrum is similar to SN 2019muj. The line profiles indicate lower velocities in SN 2020sck in comparison with SN 2005hk and SN 2012Z. The comparison of SN 2020sck

Table 4
SYN++ Fit to the Pre-maximum Spectrum of SN 2020sck

Phase*: + 1.4 days v_{phot} : 5000 km s ⁻¹ T_{BB} : 10500 K													
Parameters	C II	C III	O I _{PV}	O I _{DF}	Na I	Si II	Si III	S II	Ca II	Sc II	Fe II	Fe III	Co II
log (tau)	-1.5	-1.4	-1.0	-1.2	-1.8	-1.1	-1.1	-1.2	-0.1	-1.5	-0.9	-0.9	-0.9
v_{min} (× 10 ³ km s ⁻¹)	5.0	5.0	5.0	11.0	5.0	5.0	5.0	5.0	5.0	5.0	5.0	5.0	5.0
v_{max} (× 10 ³ km s ⁻¹)	7.0	8.0	15.0	15.0	10.0	12.0	7.0	7.0	8.0	7.0	7.0	8.0	7.0
aux (× 10 ³ km s ⁻¹)	9.0	3.0	4.5	3.0	5.0	2.5	5.0	5.0	4.0	2.5	5.0	4.0	5.0
T_{exc} (× 10 ³ K)	15	15	10	10	10	7	13	5	5	15	10	10	10

Notes. *Time since *B*-band maximum (JD 2,459,098.84). v_{phot} : the photospheric velocity (km s⁻¹). T_{BB} : the blackbody continuum temperature (K).

with other SNe Iax around maximum is shown in panel (b) of Figure 11.

Post-maximum, the Si II ($\lambda 6355$) gets weakened and Fe II lines dominate (panel (c) of Figure 11). The opacity of the Fe III lines decrease, or Fe III evolves to Fe II due to decrease in temperature. Na I D absorption line can be seen to have developed. By ~ 2 weeks, Ca II NIR triplet absorption feature gets stronger. At around +23 days post-maximum, lines due to Cr II (~ 4600 Å), Fe II (~ 5200 Å), Co II ($\sim 5900, 6500$ Å), and Fe II ($\sim 6100, 7000$ Å) can be clearly identified. In the post-maximum phase ($\sim +10.5$ days), the spectrum of SN 2020sck has more similarity with SN 2005hk. While SN 2019muj shows features due to Fe II and Co II beyond 6500 Å, those are absent in SN 2020sck. This indicates that SN 2020sck has higher temperature than SN 2019muj in this phase.

The velocity evolution provides clues to the distribution of the elements in the ejecta and hence the explosion physics. The velocity of the spectral lines of SN 2020sck has been measured by fitting a Gaussian function to the absorption minimum of the corresponding lines. In the pre-maximum phase we fit Gaussian functions to Fe III ($\lambda 4420$), Fe III ($\lambda 5156$), and Si II ($\lambda 6355$). We find the velocity of Si II to be 5712 ± 200 km s⁻¹ and that of Fe III ($\lambda 4420$) and Fe III ($\lambda 5156$) to be 6610 ± 180 km s⁻¹ and 6649 ± 200 km s⁻¹ respectively. The Fe lines have velocities ~ 800 km s⁻¹ higher than those of Si II. For SN 2007qd (McClelland et al. 2010) and SN 2014ck (Tomasella et al. 2016), the Fe lines are 800 and 1000 km s⁻¹ higher than Si II respectively. This trend has been also seen for other SNe Iax—like SN 2005hk (Phillips et al. 2007) and SN 2010ae (Stritzinger et al. 2014). This observation implies that fully burned materials are present in all the layers in the ejecta and that it supports an explosion mechanism that produces extensive mixing (Phillips et al. 2007). Around maximum, the velocity of Si II, C II ($\lambda 6580$), and Ca II ($\lambda 3945$) are 5185 km s⁻¹, 5211 km s⁻¹, and 5308 km s⁻¹ respectively. However, the velocity of Fe III ($\lambda 5156$) is 5558 ± 170 km s⁻¹. The velocity of Fe III ($\lambda 4420$) cannot be measured, as it gets blended with other lines around the maximum. To understand the density profile and distribution of elements in the ejecta, we compare the observed spectrum of SN 2020sck with synthetic spectrum generated using SYN++ and TARDIS.

5. Spectral Modeling

The line velocities for SNe Iax are low and hence the spectral features post-maximum are easily identifiable than those for SNe Ia. The spectral features were identified using the parametrized spectrum synthesis code SYN++ (Thomas et al.

2011). The code makes simple assumptions of homologous expansion of the ejecta in a spherically symmetric distribution. A synthetic spectrum is generated by assuming a well defined sharp photosphere that emits a continuous blackbody spectrum. Line formation occurs due to resonant scattering by assuming Sobolev approximation. The code can be used for line identifications, estimating the photospheric velocity and the velocity interval over which lines due to each ion are formed. The fit parameters are the temperature of the blackbody continuum (T_{BB}), velocity of the photosphere (v_{phot}), the minimum and maximum velocity of the line forming region (v_{min} & v_{max}), the optical depth of the ions (τ), the Boltzmann excitation temperature (T_{exc}), and the e-folding velocity (aux). A line is considered to be detached if the minimum velocity exceeds the photospheric velocity. The spectrum at +1.4 days has been compared with the synthetic spectrum to identify the lines and estimate the velocities.

The spectrum at +1.4 days was fit with a photospheric velocity (v_{phot}) of 5000 km s⁻¹ and a blackbody temperature (T_{BB}) of 10,500 K. The spectrum has been fit with C II, C III, and O I, IMEs like Na I, Si II, Si III, S II, and Ca II, and IGEs like Sc II, Fe II, Fe III, and Co II. To fit the broad O I absorption feature around ~ 7600 Å, we used a photospheric component and a detached component at 11,000 km s⁻¹. The velocity of the line forming region of C II, Si III, S II, Sc II, Fe II, and Co II is between 5000 km s⁻¹ (v_{min}) and 7000 km s⁻¹ (v_{max}). The velocity of C III and Fe III is between 5000 and 8000 km s⁻¹. The Si II line has been fit with a velocity range of 5000–12,000 km s⁻¹. This velocity range of IMEs and IGEs show that the ejecta is mixed. To fit the C II and C III line profiles, an excitation temperature of 15,000 K has been used. The details of the fit are provided in Table 4. The detection of unburned carbon is of extreme importance as it can put constraint on the explosion mechanism as well as the progenitor system. The presence of C II, C III and O I features hint toward thermonuclear explosion in a C–O white dwarf (Foley et al. 2010a) in contrast to O–Ne–Mg white dwarf (Nomoto et al. 2013). The feature due to C III ($\lambda 4647$) was also reported in SN 2014ck (Tomasella et al. 2016). Sc II feature was also identified in SN 2007qd (McClelland et al. 2010), SN 2008ha (Foley et al. 2009), SN 2010ae (Stritzinger et al. 2014), SN 2014ck (Tomasella et al. 2016). All the major features are reproduced well in the synthetic spectrum. Figure 12 shows the SYN++ fit to the +1.4 days spectrum of SN 2020sck.

In order to put constraint on the explosion mechanism, perform line identification, estimate the abundance of the various elements ejected and get a knowledge of the ionization state of the ejecta we compare the observed spectrum of

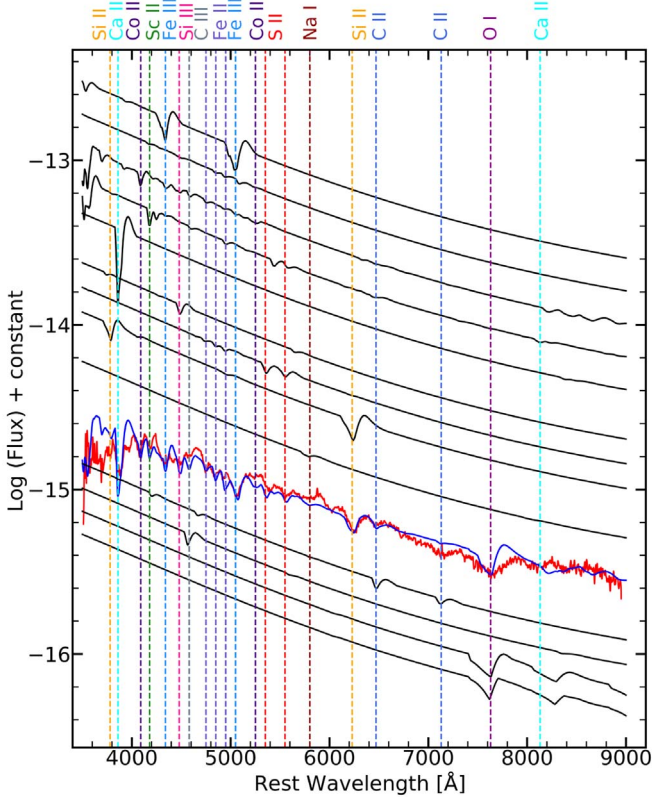


Figure 12. Dereddened and redshift corrected spectra of SN 2020sck at +1.4 days since B -band maximum (shown in red). Overplotted in blue is the synthetic spectra calculated using `SYN++`. The contributions from each ion are shown by dashed vertical lines. The observed spectrum has been smoothed for visual clarity.

SN 2020sck at -5.5 days, $+1.4$ days, and $+10.4$ days since the B -band maximum with synthetic spectrum generated using 1D Monte Carlo radiative transfer code `TARDIS` (Kerzendorf & Sim 2014). To generate a synthetic spectrum, `TARDIS` takes as input the luminosity of the SN (L_{SN} in $\log L_{\odot}$), the time since explosion (t_{exp} in days), a density profile (density as a function of velocity), and uniform/stratified abundance. It assumes spherical symmetry, homologous expansion, a sharp well-defined photosphere and that the material in the computational domain defined by v_{inner} and v_{outer} is in radiative equilibrium. This makes the application of `TARDIS` limited to the photospheric phase. A synthetic spectrum is generated by considering a large number of Monte Carlo packets and tracing their propagation taking into account the interaction they make with the surrounding medium.

For generating the synthetic spectra, we considered the angle-averaged density profile of the three-dimensional pure deflagration explosion simulation (N5-def, Fink et al. 2014). In the N5-def explosion model, Fe and ^{56}Ni are distributed to the outer parts of the ejecta. C and O are distributed in the entire ejecta and not limited to the outer regions. This indicates a mixed composition. We considered a uniform mass fraction of elements in the ejecta throughout the velocity interval.

For comparing the observed spectrum at -5.5 days, we generate the synthetic spectrum with $t_{\text{exp}} = 12.0$ days, $L_{\text{SN}} = 8.95 \log L_{\odot}$ and a velocity interval of 8000 (v_{inner})– $12,000$ (v_{outer}) km s^{-1} (see panel (a) of Figure 15). However, we find that the absorption features are very strong. Also, the continuum seems to be bluer. This could be due to the higher

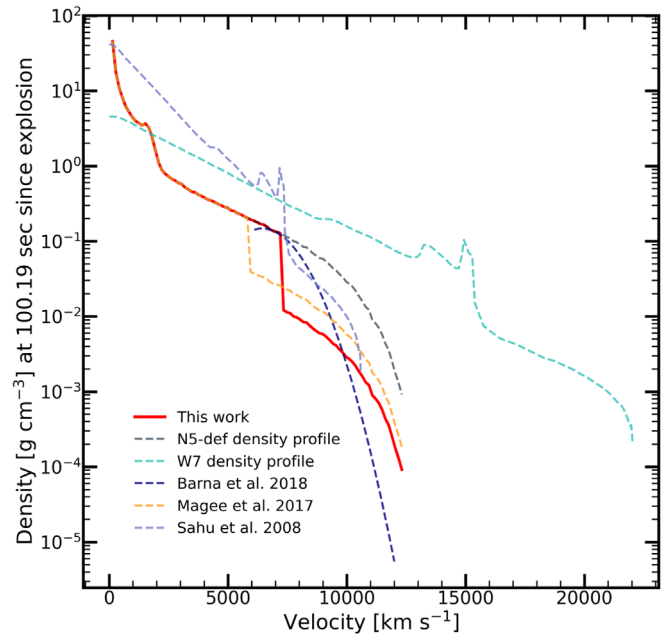


Figure 13. Density against velocity plot (in red) used in `TARDIS` for generating the synthetic spectrum. The density is similar to N5-def density profile below 7200 km s^{-1} and N5-def $\rho \times 0.1$ for velocity above 7200 km s^{-1} . Also plotted for comparison—N5-def profile (Fink et al. 2014), W7 profile (Nomoto et al. 1984), density profile for SN 2005hk from Sahu et al. 2008 and Barna et al. (2018), density profile used for the study of PS1-12bwh (Magee et al. 2017).

density in the ejecta. Decreasing the v_{inner} increases the optical depth further and increases the line strengths. We then fit the spectra, by considering a modified version of the N5-def density profile and a velocity interval of 6800 – $12,000 \text{ km s}^{-1}$. In this case, the density profile in the outer ejecta ($v > 7200 \text{ km s}^{-1}$) has been reduced (N5-def $\rho \times 0.1$). This steep change in the density profile has been supported by other studies (Sahu et al. 2008; Magee et al. 2017; Barna et al. 2018). The innermost regions of the ejecta are denser as compared to the outermost region. In Figure 13 we compare the density profile used for SN 2020sck with the N5-def density profile (Fink et al. 2014) and W7 profile (Nomoto et al. 1984). We also show the density profiles used for the study of SN 2005hk (Sahu et al. 2008; Barna et al. 2018), PS1-12bwh (Magee et al. 2017). In the case of SN 2005hk, Sahu et al. (2008) homologously scaled the density profile to increase the density in the inner regions, while Barna et al. (2018) used an exponential density profile with a cut-off velocity v_{cut} chosen to match the deflagration density profiles. In PS1-12bwh, Magee et al. (2017) used N5-def density profile for velocity lower than 5800 km s^{-1} and N5-def $\rho \times 0.2$ for velocities above 5800 km s^{-1} .

A uniform composition of elements throughout the entire ejecta ($v \geq v_{\text{inner}}$) is supported by the mixed abundance structure in pure deflagration models. The `syn++` synthetic spectrum also indicates the elements are distributed throughout the entire ejecta. In this case, we find the photospheric temperature to be $t_{\text{inner}} = 11287 \text{ K}$, which is similar to that found by fitting a blackbody to the photometric spectral energy distribution (11037 K). The synthetic spectrum reproduces the more prominent lines due to Ca II (H & K), Fe III ($\lambda 4420$), Fe III ($\lambda 5156$), S II and Si II ($\lambda 6355$). The C II ($\lambda 6578$) feature is reproduced with a mass fraction $X(\text{C}) = 0.003$ while it is 0.114 in the N5-def model (Fink et al. 2014).

Table 5
Fit Parameters of TARDIS Model and Comparison of Ejecta Composition with N5-def Model (Fink et al. 2014)

X(C)	X(O)	X(Si)	X(S)	X(Ca)	X(Ti)	X(Cr)	X(Co)	X(Fe)	X(Ni)
Phase*: - 5.5 days v_{inner} : 6800 km s ⁻¹ v_{outer} : 12,000 km s ⁻¹ L_{SN} : 8.95 log L_{\odot} t_{inner} : 11287 K									
0.003	0.355	0.15	0.005	0.018	0.000	0.000	0.010	0.020	0.410
Phase*: + 1.4 days v_{inner} : 6200 km s ⁻¹ v_{outer} : 12,000 km s ⁻¹ L_{SN} : 9.05 log L_{\odot} t_{inner} : 10033 K									
0.003	0.355	0.15	0.005	0.018	0.000	0.000	0.010	0.020	0.410
Phase*: + 10.4 days v_{inner} : 5800 km s ⁻¹ v_{outer} : 12,000 km s ⁻¹ L_{SN} : 8.85 log L_{\odot} t_{inner} : 7780 K									
0.003	0.200	0.080	0.005	0.018	0.020	0.020	0.010	0.180	0.410
N5-def model mean abundances									
0.114	0.157	0.065	0.023	0.003	0.00	0.00	0.009	0.01	0.427

Notes. * Time since *B*-band maximum (JD 2,459,098.84); v_{inner} : Inner velocity of the ejecta (km s⁻¹). v_{outer} : Outer velocity of the ejecta (km s⁻¹); L_{SN} : Luminosity of the SN (log L_{\odot}). t_{inner} : Temperature of the photosphere (K).

To further investigate the effect of the density profile and the abundance structure, we compare the spectrum at +1.4 days with a synthetic spectrum generated with $t_{\text{exp}} = 18.0$ days, $L_{\text{SN}} = 9.05 \log L_{\odot}$ and a velocity interval of 6200 (v_{inner})–12,000 (v_{outer}) km s⁻¹. We used the same mass fraction for the elements. The photospheric temperature (t_{inner}) is 10,033 K. This matches well with that found from the synthetic spectrum generated by SYN++, $T_{\text{phot}} = 10,500$ K. Here also, the absorption features due to C, Si, S, Fe and Ca are reproduced well in the spectrum. However, the absorption feature around ~ 4200 Å due to Co are not reproduced (panel (b) in Figure 15).

The synthetic spectrum at +10.4 days has been generated with $t_{\text{exp}} = 26.0$ days, $L_{\text{SN}} = 8.85 \log L_{\odot}$ and a velocity interval of 5800 (v_{inner})–12,000 (v_{outer}) km s⁻¹. The photospheric temperature is 7780 K. In this model, we consider two cases —(i) With Ti and Cr in the ejecta and (ii) Without Ti and Cr (panel (c) in Figure 15). Introducing Ti and Cr reduces the flux in the bluer region around ~ 4300 Å. In this phase we increase the mass fraction of Fe from X(Fe)=0.02 to X(Fe)=0.18. Similarly, we decrease the mass fraction of Si from X(Si)=0.15 to X(Si)=0.08. This means that the ejecta is entering into an Fe dominated phase. The absorption features due to Fe II ($\lambda 4549$), Fe II ($\lambda 5018$), Fe II ($\lambda 6149$), Fe II ($\lambda 6247$), Fe II ($\lambda 6456$), C II ($\lambda 6578$), O I ($\lambda 7774$), and Ca II-IR triplet are reproduced in the synthetic spectrum also.

While three-dimensional deflagration models predict a mixed abundance structure, Barna et al. (2018) made a template based approach with stratified abundance structure to explore the ejecta of several bright SNe Iax. In the template model, the mass fraction of the IGE's and IME's decreases with velocity and C is tolerated only in the outermost regions. However, in this work we model the spectra using the same mass fraction over the velocity interval for the elements in the ejecta. This is in close resemblance to the three-dimensional hydrodynamic simulations. Table 5 lists the mass fractions of the elements used in the synthetic spectrum and comparison with the N5-def model mean abundances (Fink et al. 2014). In Figure 14 we compare the uniform abundance of the elements in the ejecta of SN 2020sck with the stratified abundance structure for SN 2005hk (Barna et al. 2018).

From the TARDIS models, we find that the density in the inner regions is higher than the outer regions. From the SYN++

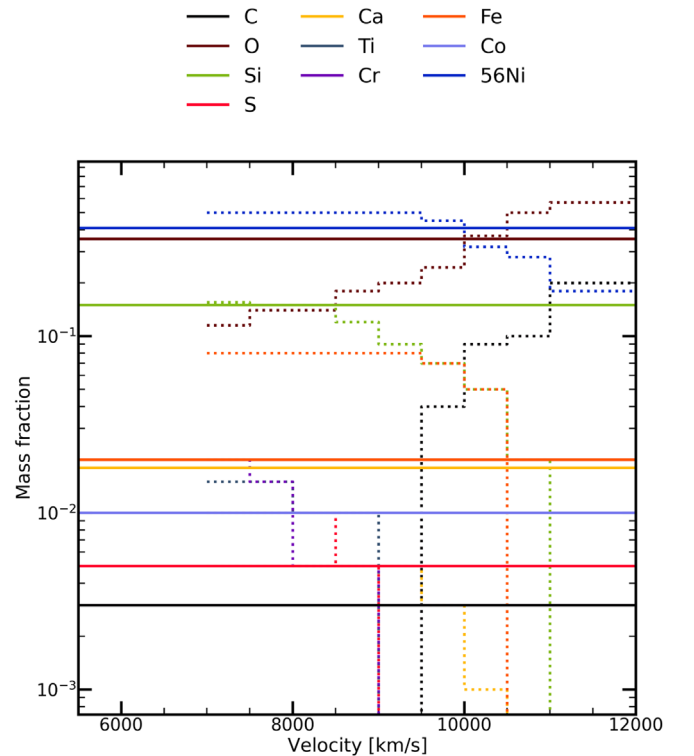


Figure 14. Comparison of the uniform abundance of elements used for SN 2020sck with the stratified abundance for SN 2005hk (Barna et al. 2018). The solid lines show the mass fractions of the elements in the ejecta of SN 2020sck while the dotted lines in the same color shows the mass fraction in the ejecta of SN 2005hk.

synthetic spectrum we find that C, O and Fe group elements are located in the ejecta between 5000 and 8000 km s⁻¹. Using a uniform composition of the elements between 5800 and 12,000 km s⁻¹ in the ejecta we confirm that most of the prominent features of C, O, Fe, Si and Ca can be reproduced in the TARDIS synthetic spectrum as well. However, some features due to C III (~ 4600 Å), Co II (~ 4100 Å), Fe II (~ 4800 Å) are reproduced well in the SYN++ model but not in the TARDIS model. The analyses presented here indicate the elements in the ejecta of SN 2020sck are mostly mixed and

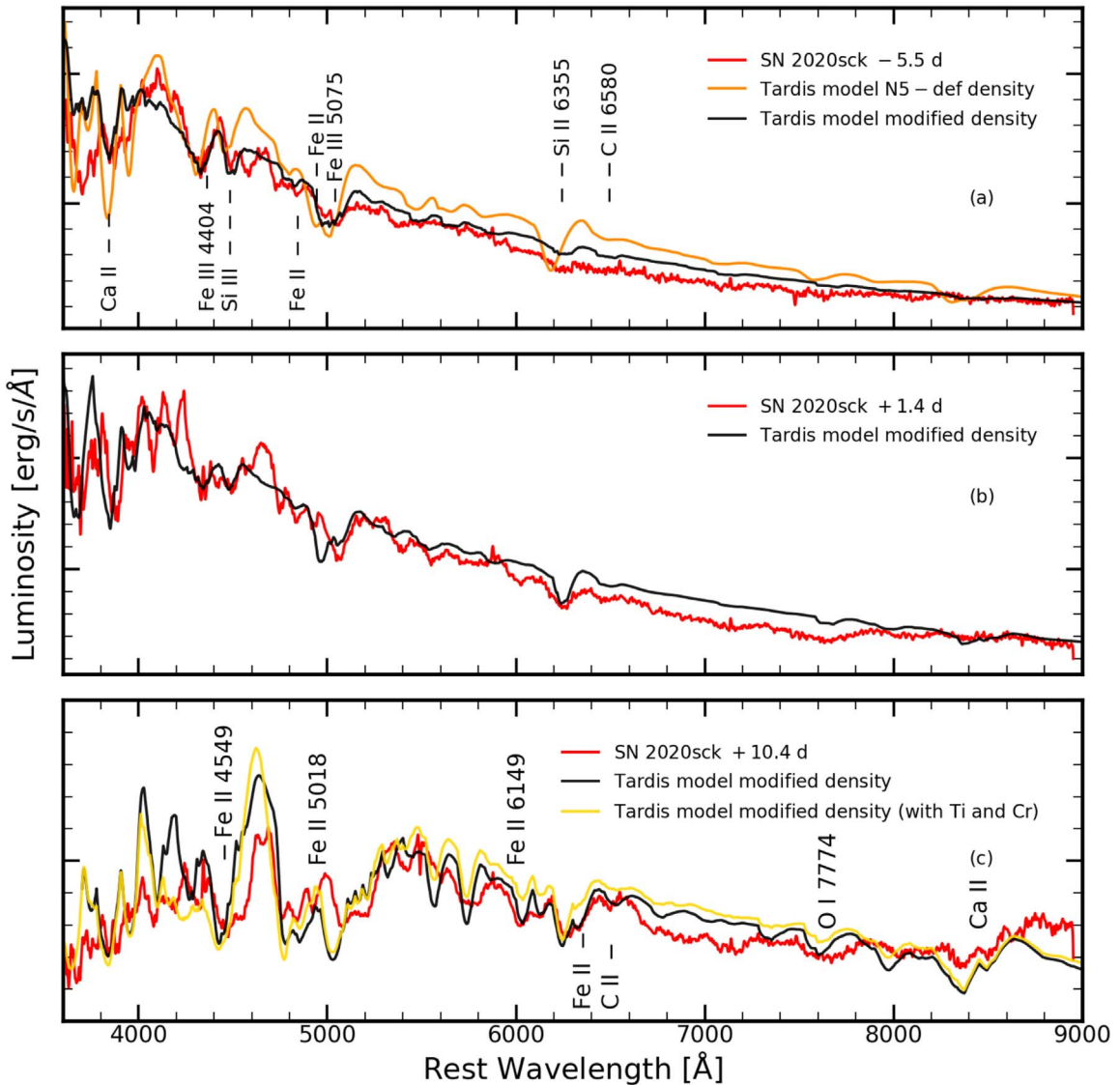


Figure 15. Panel (a) Spectrum of SN 2020sck at -5.5 days plotted along with synthetic spectrum generated using TARDIS with N5-def density profile (darkorange) and a modified N5-def density profile (black). Panel (b) The $+1.4$ days spectrum of SN 2020sck plotted along with synthetic spectrum generated using the modified N5-def density profile. Panel (c) Postmaximum $+10.4$ days spectrum of SN 2020sck compared with synthetic spectrum generated using N5-def modified density profile without (black) and with (gold) Ti and Cr. The angle-averaged density profile has been obtained from the Heidelberg Supernova Model Archive (HESMA). The observed spectra of SN 2020sck have been smoothed.

support an explosion that is probably due to pure deflagration of a C–O white dwarf.

6. Host Galaxy

The metallicity of the host galaxy 2MASX J01103497 +0206508 can be determined from the narrow emission features in the SN spectrum. We fit Gaussian profiles to the narrow $H\alpha$ ($\lambda 6563$) and $[N\text{ II}]$ $\lambda 6583$. Using the empirical relation derived by Pettini & Pagel (2004) with the N2 index ($\log \frac{[N\text{ II}] \lambda 6583}{H\alpha \lambda 6563}$), we find the oxygen abundance to be $12 + \log(O/H) = 8.54 \pm 0.05$ dex. Metallicity values of a handful of SNe Iax have been obtained using the same relation of Pettini & Pagel (2004)—SN 2008ha, SN 2010ae, SN 2012Z, PS1-12bwh, and SN 2019gsc. These metallicity values for the comparison SNe are also listed in Table 3. SN 2008ha ($L_{\text{peak}} = 9.5 \times 10^{40}$ erg s $^{-1}$) and SN 2019gsc ($L_{\text{peak}} = 7.4 \times 10^{40}$ erg s $^{-1}$) have metal-poor environments and low peak

luminosity. There could be a relation between metallicity of the host galaxy and peak supernova magnitude, with low luminosity SNe Iax having lower metallicity (Figure 16). However, there exist no clear correlation that demonstrates that SNe Iax tend to form in sub-/supersolar-metallicity environments (Magee et al. 2017).

Using the spectrum at $+23$ days from the B -band maximum obtained with a $1.92''$ slit, we find the star formation (SFR) of the H II region near the SN. From the luminosity of the $H\alpha$ ($\lambda 6563$) line, we derive a SFR (Kennicutt 1998) of $0.09 M_{\odot} \text{ yr}^{-1}$. Young massive stars ($\geq 10 M_{\odot}$) mostly contribute to the integrated line flux. From the forbidden $[O\text{ II}](\lambda 3727)$ line luminosity, we derive a star formation rate of $0.02 M_{\odot} \text{ yr}^{-1}$. The SFR derived from $[O\text{ II}]$ is less precise and suffers from systematic errors due to extinction (Kennicutt 1998). In comparison, Foley et al. (2009) derived a star formation rate of $0.07 M_{\odot} \text{ yr}^{-1}$ for the host galaxy of SN 2008 ha using far-infrared luminosity.

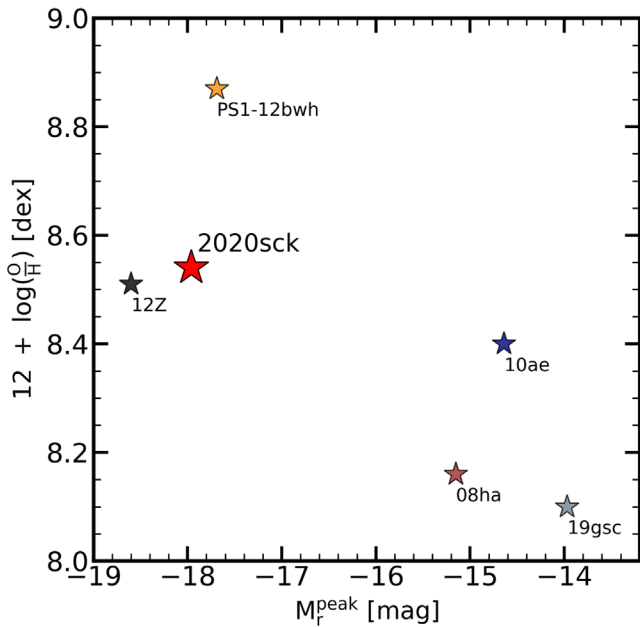


Figure 16. $12 + \log(\text{O}/\text{H})$ plotted against peak magnitude in r -band for a sample of SNe Iax. The luminous objects have higher oxygen abundance.

7. Explosion Models

Considering the single degenerate M_{ch} white dwarf explosion, we discuss three models based on the propagation of the burning front through the white dwarf to explain the explosion of SN 2020sck and similar SNe Iax.

First, we consider the deflagration-to-detonation (DDT) transition models. In these models the deflagration flame transitions into a detonation due to turbulent velocity fluctuations. In three-dimensional simulations of M_{ch} white dwarfs, a range of observed luminosity can be produced (Seitenzahl et al. 2013; Sim et al. 2013). By varying the deflagration strength and central density of the white dwarf, a set of models have been generated that can account for the observed properties of SNe Ia. In this set of models, the explosions have been generated by considering a distribution of ignition points. The models with greater deflagration strengths produce a lesser amount of ^{56}Ni because the white dwarf expands more before detonation sets in. The models produce a range of ^{56}Ni mass of $0.32\text{--}1.1 M_{\odot}$. This mass range is higher than that found for SN 2020sck ($0.13 M_{\odot}$). We also considered a sample of SNe Iax and constructed the quasi-bolometric light curve (3000–9500 Å). The quasi-bolometric light curves have been fit with the modified radiation diffusion model (Equation (2)). Table 6 shows the fit parameters of the radiation diffusion model to the SNe Iax sample considered here, and Figure 17 shows the fit of Equation (2) to the quasi-bolometric light curves of the sample. The range of ^{56}Ni ($0.004 M_{\odot}\text{--}0.17 M_{\odot}$) estimated from the fitting is lower than that inferred from the DDT models. The kinetic energy produced by the DDT models ($E_{\text{K}}=1.20\text{--}1.67 \times 10^{51}$ erg) is also higher than that observed for SNe Iax. Through our fit to the bolometric light curve, we find the range of kinetic energy between 0.003×10^{51} erg (SN 2008ha)– 0.39×10^{51} erg (SN 2012Z). The peak magnitude for the DDT model with the weakest deflagration N1 (with one ignition spot) is $M_B = -19.93$. But, the model with the strongest deflagration N1600 (with 1600 deflagration spots and a central density $\rho_c = 2.9 \times 10^9 \text{ gm cm}^{-3}$) can produce the luminosity of $M_B = -18.26$ mag observed in the brighter Iax.

However, the IME production for model N1600 is too large ($M(\text{Si})=0.36 M_{\odot}$) and the velocity higher compared to SNe Iax. The $(B - V)$ color for the DDT models at B -maximum is too red ($0.15 \text{ mag}\text{--}0.56 \text{ mag}$) compared to SN 2020sck ($B - V) = -0.08 \text{ mag}$). The DDT models do not seem to reproduce most of the observed properties of explosion for SN 2020sck and the sample SNe Iax.

Next, we consider the pulsational delayed detonation (PDD) model. Due to slow deflagration in a white dwarf, it expands but remains bound. As the burning stops, the infalling C–O layer compresses the IGE-rich mixed layers. As a result, detonation is triggered by compression and ignition (Khokhlov 1991; Hoefflich et al. 1995). In the one-dimensional case, several models have been generated by varying the transition density. This gives rise to a range of ^{56}Ni mass ($0.12\text{--}0.66 M_{\odot}$). The ^{56}Ni mass found for SN 2020sck matches with the model PDD5 (the transition density for this model at which the deflagration is turned to detonation is $\rho_{\text{tr}} = 0.76 \times 10^7 \text{ gm cm}^{-3}$) for which the amount of ^{56}Ni produced is $0.12 M_{\odot}$. However, the average expansion velocity for this model is 8400 km s^{-1} . This is higher than that found in SN 2020sck ($\sim 5000 \text{ km s}^{-1}$). The $(B - V)$ color in the PDD5 model is 0.44 mag , which is redder than that for SN 2020sck (-0.08 mag).

In the PDD models, the kinetic energy varies from $0.34\text{--}1.52 \times 10^{51}$ erg. The range of velocity and hence kinetic energy is also observed in SNe Iax. The extreme case PDD535 ($\rho_{\text{tr}}=0.45 \times 10^7 \text{ gm cm}^{-3}$; Hoefflich et al. 1995) has low ^{56}Ni mass ($0.16 M_{\odot}$) and low average expansion velocities $\sim 4500 \text{ km s}^{-1}$. Due to the pulsation, the material that is falling back interacts with the outgoing detonation wave front. As a result, a dense shell of mass is formed surrounded by fast-moving layers. These fast-moving layers take away some kinetic energy and decelerate the inner parts of the expanding ejecta. This result in lower expansion velocities. However, in the case of PDD535, the Fe and Ni layers are located below 4000 km s^{-1} . By comparing the synthetic spectra with the observations of SN 2020sck, we find that the Fe and Ni line forming layers are present in the outer parts of the ejecta ($\geq 7000 \text{ km s}^{-1}$). The $(B - V)$ color is 0.60 mag , which is redder than that for SN 2020sck. Hence, the PDD models also do not reproduce some of the observed properties of SN 2020sck.

Previous study by Fink et al. (2014) have shown that most of the observed properties of SNe Iax class (brighter and intermediate luminosity) can be successfully described by pure deflagrations of M_{ch} C–O white dwarf. Fink et al. (2014) have generated a set of models by varying the deflagration strength (changing the number of ignition spots). These models produce a range of ^{56}Ni mass ($0.03\text{--}0.34 M_{\odot}$), with the peak B -band magnitude varying from -16.55 (N1) to -18.11 (N1600). The models also produce mixed abundance distribution in which Fe and Ni can be present in the outer layers of the ejecta. Models with weak and intermediate deflagration strengths (N1–N100) produce lesser ejecta and a bound remnant. Comparing with the various models, we find that the explosion properties of the N5-def model with five ignition points (with the central density of the white dwarf being $\rho_c = 2.9 \times 10^9 \text{ gm cm}^{-3}$) matches well with that found by fitting the bolometric light curve of SN 2020sck with the radiation diffusion model. Also, the N5-def density profile with a steep decrease in the outer layers can successfully reproduce the observed spectral features. The rise-times to B -maximum for the pure deflagration models are less

Table 6
Fit Parameters of 1D Radiation Diffusion Model (Equation (2)) to the Sample of SNe Iax

SN	M_{Ni} (M_{\odot})	t_{ic} (days)	t_{γ} (days)	JD_{exp}	M_{ej} (M_{\odot})	v_{exp} (km s^{-1})	E_{K} ($\times 10^{51}$ erg)
SN 2002cx	$0.07^{+0.01}_{-0.01}$	$12.29^{+2.12}_{-1.78}$	$42.6^{+3.1}_{-4.2}$	$2452402.43^{+1.12}_{-1.85}$	$0.69^{+0.20}_{-0.24}$	6000	$0.15^{+0.04}_{-0.05}$
SN 2005hk	$0.14^{+0.01}_{-0.01}$	$15.00^{+1.84}_{-1.58}$	$52.8^{+4.3}_{-2.9}$	$2453669.65^{+1.02}_{-1.17}$	$1.13^{+0.27}_{-0.23}$	6500	$0.29^{+0.06}_{-0.06}$
SN 2008 ha	$0.004^{+0.000}_{-0.000}$	$9.30^{+1.79}_{-0.52}$	$27.3^{+0.1}_{-0.2}$	$2454773.02^{+0.36}_{-2.03}$	$0.13^{+0.04}_{-0.01}$	2000	$0.003^{+0.0009}_{-0.0003}$
SN 2010ae	$0.006^{+0.001}_{-0.001}$	$5.43^{+1.79}_{-0.52}$	$38.5^{+2.9}_{-1.5}$	$2455246.48^{+0.5}_{-1.1}$	$0.13^{+0.08}_{-0.02}$	5500	$0.02^{+0.01}_{-0.00}$
SN 2012Z	$0.17^{+0.01}_{-0.01}$	$12.97^{+0.66}_{-0.50}$	$44.4^{+1.2}_{-1.2}$	$2455954.32^{+0.31}_{-0.37}$	$1.04^{+0.1}_{-0.09}$	8000	$0.39^{+0.08}_{-0.14}$
SN 2014ck	$0.03^{+0.01}_{-0.01}$	$8.32^{+0.58}_{-0.57}$	$39.6^{+1.9}_{-1.4}$	$2456835.55^{+0.25}_{-0.24}$	$0.16^{+0.02}_{-0.02}$	3000	$0.009^{+0.001}_{-0.001}$
SN 2014ek	$0.12^{+0.01}_{-0.01}$	$16.10^{+1.21}_{-2.41}$	$27.0^{+1.37}_{-0.37}$	$2456944.12^{+1.39}_{-0.63}$	$0.90^{+0.14}_{-0.27}$	4500	$0.11^{+0.02}_{-0.03}$
SN 2019gsc	$0.0019^{+0.000}_{-0.000}$	$9.85^{+0.25}_{-0.26}$	$42.9^{+0.37}_{-0.43}$	$2458627.24^{+0.3}_{-0.3}$	$0.26^{+0.098}_{-0.084}$	3500	$0.019^{+0.007}_{-0.006}$
SN 2019muj	$0.017^{+0.001}_{-0.001}$	$6.2^{+0.63}_{-0.93}$	$28.4^{+0.65}_{-0.70}$	$2458699.52^{+0.65}_{-0.46}$	$0.14^{+0.05}_{-0.03}$	5000	$0.024^{+0.006}_{-0.005}$

Notes. All the parameters are explained in Section 3.3.

Table 7
Comparing the Explosion Properties of SN 2020sck with Single Degenerate M_{ch} White Dwarf Explosion Models

Explosion Model	Velocity	Peak Magnitude	Color	Rise-Time	Spectra	^{56}Ni	Ref.
Deflagration-to-Detonation	×	×	×	✓	×	×	1
Pulsational Delayed Detonation (Except PDD5 and PDD535)	×	×	×	✓	×	×	2
PDD5	×	✓	×	×	×	✓	2
PDD535	×	✓	×	×	×	✓	2
Pure Deflagration (N5-def)	✓	✓	✓	×	✓	✓	3

References: (1) Seitzzahl et al. (2013), Sim et al. (2013); (2) Hoefflich et al. (1995); (3) Fink et al. (2014). If the model matches the observed property of SN 2020sck, we put a ✓, else we put a ×.

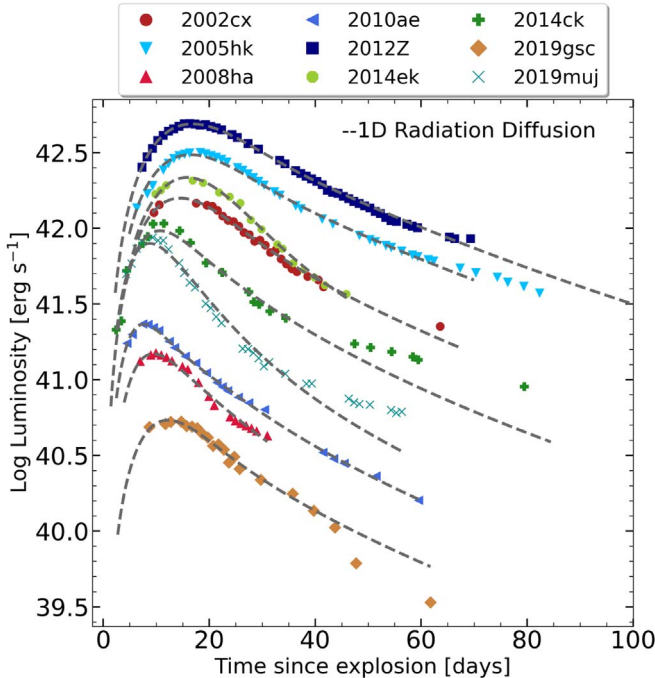


Figure 17. 1D radiation diffusion model fit to a sample of SNe Iax. A quasi-bolometric light curve has been constructed by integrating the flux from 3000 Å to 9500 Å for all objects. See Table 6 for the fit parameters.

(7.6 d—14.4 d) compared to SN 2020sck, but fit the range observed in the sample SNe Iax.

In Table 7, we compare various explosion scenarios of single degenerate M_{ch} white dwarfs and show which model can best

explain the observed properties of SN 2020sck and the sample SNe Iax. Based on this, like in the previous studies by Li et al. (2003), Phillips et al. (2007); Fink et al. (2014) we conclude that the pure deflagration models explain most of the observed parameters of SNe Iax.

8. Summary

In this work we establish that SN 2020sck is a supernova of type Iax with a $\Delta m_B(15) = 2.03 \pm 0.05$ mag and $M_B = -17.81 \pm 0.22$ mag. From the pre-maximum observations in the ZTF $-g$ band, we constrained the date of explosion as 2020 August 20 (JD = 2,459,082.4). The light curves in R and I bands do not show any secondary maximum. The $(B - V)$ color at maximum is -0.08 mag, which is bluer compared to the sample of SNe Iax. By fitting the quasi-bolometric light curve as well as the blackbody corrected bolometric light curve of SN 2020sck with 1D radiation diffusion model we find $0.13 M_{\odot}$ and $0.17 M_{\odot}$ of ^{56}Ni respectively. By comparing the quasi-bolometric light curve with angle-averaged bolometric light curve from three-dimensional pure deflagration models of C–O white dwarfs with varying deflagration strengths, we find similarity of SN 2020sck with N5-def model (Fink et al. 2014). The mass ejected in the explosion is $0.34 M_{\odot}$ with a kinetic energy of 0.05×10^{51} erg.

The spectral characteristics of SN 2020sck are similar to SN 2005hk and SN 2019muj. The comparison of the near-maximum spectrum of SN 2020sck with SYN++ shows the presence of higher ionization states of elements like C III, Si III, and Fe III, indicating a hot photosphere. The presence of unburned C and O points toward a C–O white dwarf progenitor. Fe lines are found at higher velocities than IME’s indicating that the ejecta is mixed. Angle-averaged one-dimensional density

profile of pure deflagration explosion of M_{ch} white dwarf with a steep decrease in the outer layers of the ejecta can successfully reproduce the prominent absorption features in the spectra of SN 2020sck. The metallicity of the host galaxy of SN 2020sck is similar to SN 2012Z (Yamanaka et al. 2015), which exploded in a spiral galaxy. More studies of SNe Iax will help to understand the correlation with their host galaxy environment.

We thank the anonymous referee for carefully going through the manuscript and providing detailed comments that helped in improving the content of the paper. We thank the staff of IAO, Hanle and CREST, Hosakote that made the observations possible. This work made use of data from the GROWTH-India Telescope (GIT) setup by the Indian Institute of Astrophysics (IIA) and the Indian Institute of Technology Bombay (IITB) with funding from DST-SERB and IUSSTF. It is located at IAO. We acknowledge funding by the IITB alumni batch of 1994, which partially supports operations of the telescope. The facilities at IAO and CREST are operated by the Indian Institute of Astrophysics, Bengaluru, an autonomous Institute under Department of Science and Technology, Government of India. We also thank the observers of HCT who shared their valuable time for Target of Opportunity (ToO) observations during the initial follow up. HK thanks the LSSTC Data Science Fellowship Program, which is funded by LSSTC, NSF Cybertraining grant #1829740, the Brinson Foundation, and the Moore Foundation; his participation in the program has benefited this work. Nayana A.J. would like to acknowledge DST-INSPIRE Faculty Fellowship (IFA20-PH-259) for supporting this research. This work is also based on observations obtained at the 3.6 m Devasthal Optical Telescope (DOT), which is a National Facility run and managed by Aryabhata Research Institute of Observational Sciences (ARIES), an autonomous Institute under Department of Science and Technology, Government of India. This work has made use of the NASA Astrophysics Data System¹² (ADS), the NASA/IPAC extragalactic database¹³ (NED) and NASA/IPAC Infrared Science Archive (IRSA)¹⁴ which is operated by the Jet

Propulsion Laboratory, California Institute of Technology. We acknowledge, Weizmann Interactive Supernova Data REPOSITORY¹⁵ (WISeREP), (Yaron & Gal-Yam 2012). This research made use of TARDIS, a community-developed software package for spectral synthesis in supernovae (Kerzendorf & Sim 2014; Kerzendorf et al. 2019). The development of TARDIS received support from the Google Summer of Code initiative and from ESA’s Summer of Code in Space program. TARDIS makes extensive use of Astropy and PyNE. This work made use of the Heidelberg Supernova Model Archive (HESMA).¹⁶ The analysis has made use of the following software and packages—(i) *Image Reduction and Analysis Facility* (IRAF), Tody (1993); (ii) PyRAF, Science Software Branch at STScI (2012); (iii) NumPy, Van Der Walt et al. (2011); (iv) Matplotlib, Hunter (2007); (v) Scipy, Virtanen et al. (2020); (vi) pandas, v (2020); (vii) Astropy, Astropy Collaboration et al. (2013); (viii) emcee, Foreman-Mackey et al. (2013); (ix) Corner, Foreman-Mackey (2016); (x) SYN++, Thomas et al. (2011); (xi) TARDIS, Kerzendorf & Sim (2014); (xii) scikit-learn, Pedregosa et al. (2011).

Data Availability

The observed data (reduced) presented in this work and also the results of the analyses obtained based on open-source resources like TARDIS, syn++ will be made available online at Zenodo <https://doi.org/10.5281/zenodo.5619721>. The reduced spectra will also be made available in the WISeREP archive (Yaron & Gal-Yam 2012). Raw data (observed) can be made available by the first author on reasonable request.

Appendix A Tables

UBVRI magnitudes of the standard stars in the field of SN 2020sck are given in Table 8. In Table 9 we present the log of the spectroscopic observations of SN 2020sck made with HCT.

Table 8
UBVRI Magnitudes of Local Standards in the Field of SN 2020sck

ID	<i>U</i>	<i>B</i>	<i>V</i>	<i>R</i>	<i>I</i>
1	16.156 ± 0.061	16.047 ± 0.010	15.374 ± 0.004	15.013 ± 0.009	14.592 ± 0.012
2	17.069 ± 0.061	17.019 ± 0.010	16.442 ± 0.004	16.139 ± 0.009	15.759 ± 0.012
3	18.229 ± 0.063	17.016 ± 0.010	15.544 ± 0.004	14.521 ± 0.009	13.345 ± 0.012
4	15.991 ± 0.061	15.199 ± 0.009	14.177 ± 0.004	13.639 ± 0.009	13.059 ± 0.012
5	18.522 ± 0.065	17.763 ± 0.011	16.809 ± 0.004	16.254 ± 0.009	15.685 ± 0.014
6	14.292 ± 0.061	14.235 ± 0.009	13.671 ± 0.004	13.382 ± 0.009	13.027 ± 0.011
7	15.054 ± 0.061	15.096 ± 0.009	14.513 ± 0.004	14.208 ± 0.010	13.816 ± 0.012
8	19.227 ± 0.069	17.865 ± 0.011	16.452 ± 0.004	15.560 ± 0.010	14.655 ± 0.012

¹² <https://ui.adsabs.harvard.edu/>

¹³ <https://ned.ipac.caltech.edu/>

¹⁴ <https://irsa.ipac.caltech.edu/applications/DUST/>

¹⁵ <https://wiserep.weizmann.ac.il/>

¹⁶ <https://hesma.h-its.org>

Table 9
Log of spectroscopic observations of SN 2020sck from HCT

JD (2459000+)	Date	Phase* (d)	Range (Å)
93.31	2020-08-31	-5.53	3500–7800; 5200–9100
94.27	2020-09-01	-4.57	3500–7800; 5200–9100
95.34	2020-09-02	-3.50	3500–7800; 5200–9100
100.24	2020-09-07	1.40	3500–7800; 5200–9100
101.45	2020-09-08	2.61	3500–7800
104.35	2020-09-11	5.51	3500–7800; 5200–9100
106.39	2020-09-13	7.55	3500–7800; 5200–9100
109.28	2020-09-16	10.44	3500–7800; 5200–9100
113.18	2020-09-20	14.34	3500–7800
117.31	2020-09-24	18.47	3500–7800; 5200–9100
120.40	2020-09-27	21.56	3500–7800
122.39	2020-09-29	23.55	3500–7800; 5200–9100
126.34	2020-10-03	27.50	3500–7800; 5200–9100

Notes. *Time since *B*-band maximum (JD 2,459,098.84).

ORCID iDs

Anirban Dutta  <https://orcid.org/0000-0002-7708-3831>
D. K. Sahu  <https://orcid.org/0000-0002-6688-0800>
G. C. Anupama  <https://orcid.org/0000-0003-3533-7183>
Brajesh Kumar  <https://orcid.org/0000-0001-7225-2475>
Avinash Singh  <https://orcid.org/0000-0003-2091-622X>
Varun Bhalerao  <https://orcid.org/0000-0002-6112-7609>

References

- Ahumada, R., Prieto, C. A., Almeida, A., et al. 2020, *ApJS*, 249, 3
Amett, W. D. 1982, *ApJ*, 253, 785
Astropy Collaboration, Robitaille, T. P., & Tollerud, E. J. 2013, *A&A*, 558, A33
Barna, B., Szalai, T., Kerzendorf, W. E., et al. 2018, *MNRAS*, 480, 3609
Barna, B., Szalai, T., Jha, S. W., et al. 2021, *MNRAS*, 501, 1078
Bellm, E. C., Kulkarni, S. R., Graham, M. J., et al. 2019, *PASP*, 131, 018002
Bertin, E. 2011, in ASP Conf. Ser. 442, *Astronomical Data Analysis Software and Systems XX*, ed. I. N. Evans et al. (San Francisco, CA: ASP), 435
Bessell, M. S., Castelli, F., & Plez, B. 1998, *A&A*, 333, 231
Blinnikov, S. I., Röpke, F. K., Sorokina, E. I., et al. 2006, *A&A*, 453, 229
Branch, D., Baron, E., Thomas, R. C., et al. 2004, *PASP*, 116, 903
Chatzopoulos, E., Wheeler, J. C., & Vinko, J. 2012, *ApJ*, 746, 121
Dessart, L., Blondin, S., Hillier, D. J., & Khokhlov, A. 2014, *MNRAS*, 441, 532
Dutta, A., Singh, A., Anupama, G. C., Sahu, D. K., & Kumar, B. 2021, *MNRAS*, 503, 896
Fink, M., Kromer, M., Seitenzahl, I. R., et al. 2014, *MNRAS*, 438, 1762
Firth, R. E., Sullivan, M., Gal-Yam, A., et al. 2015, *MNRAS*, 446, 3895
Fitzpatrick, E. L. 1999, *PASP*, 111, 63
Flewelling, H. 2018, AAS Meeting, 231, 436.01
Foley, R. J., Brown, P. J., Rest, A., et al. 2010a, *ApJL*, 708, L61
Foley, R. J., McCully, C., Jha, S. W., et al. 2014, *ApJ*, 792, 29
Foley, R. J., Van Dyk, S. D., Jha, S. W., et al. 2015, *ApJL*, 798, L37
Foley, R. J., Chornock, R., Filippenko, A. V., et al. 2009, *AJ*, 138, 376
Foley, R. J., Rest, A., Stritzinger, M., et al. 2010b, *AJ*, 140, 1321
Foley, R. J., Challis, P. J., Chornock, R., et al. 2013, *ApJ*, 767, 57
Foreman-Mackey, D. 2016, *JOSS*, 1, 24
Foreman-Mackey, D., Conley, A., Meierjürgen Farr, W., et al. 2013, emcee: The MCMC Hammer, *Astrophysics Source Code Library*, ascl:1303.002
Fox, O. D., Johansson, J., Kasliwal, M., et al. 2016, *ApJL*, 816, L13
Fremling, C. 2020, *Transient Name Server Discovery Report*, 2020–2629, 1
Gamezo, V. N., Khokhlov, A. M., Oran, E. S., Chetkelkhanova, A. Y., & Rosenberg, R. O. 2003, *Sci*, 299, 77
Han, Z., & Podsiadlowski, P. 2004, *MNRAS*, 350, 1301
Hoefflich, P., & Khokhlov, A. 1996, *ApJ*, 457, 500
Hoefflich, P., Khokhlov, A. M., & Wheeler, J. C. 1995, *ApJ*, 444, 831
Höfllich, P., Gerardy, C. L., Fesen, R. A., & Sakai, S. 2002, *ApJ*, 568, 791
Hoyle, F., & Fowler, W. A. 1960, *ApJ*, 132, 565
Hunter, J. D. 2007, *CSE*, 9, 90
Iben, I. J., & Tutukov, A. V. 1984, *ApJ*, 284, 719
Jha, S., Branch, D., Chornock, R., et al. 2006, *AJ*, 132, 189
Kasen, D. 2006, *ApJ*, 649, 939
Kawabata, M., Maeda, K., Yamanaka, M., et al. 2021, *PASJ*, 73, 1295
Kennicutt, R. C. J. 1998, *ARA&A*, 36, 189
Kerzendorf, W., Nöbauer, U., Sim, S., et al. 2019, tardis-sn/tardis: TARDIS v3.0 alpha2, v3.0-alpha.2, Zenodo doi:10.5281/zenodo.2590539
Kerzendorf, W. E., & Sim, S. A. 2014, *MNRAS*, 440, 387
Khokhlov, A., Mueller, E., & Hoefflich, P. 1993, *A&A*, 270, 223
Khokhlov, A. M. 1991, *A&A*, 245, L25
Kromer, M., Sim, S. A., Fink, M., et al. 2010, *ApJ*, 719, 1067
Kromer, M., Fink, M., Stanishev, V., et al. 2013, *MNRAS*, 429, 2287
Kromer, M., Ohlmann, S. T., Pakmor, R., et al. 2015, *MNRAS*, 450, 3045
Li, L., Wang, X., Zhang, J., et al. 2018, *MNRAS*, 478, 4575
Li, W., Filippenko, A. V., Chornock, R., et al. 2003, *PASP*, 115, 453
Liu, Z.-W., Zhang, J. J., Ciabattari, F., et al. 2015, *MNRAS*, 452, 838
Maeda, K., & Terada, Y. 2016, *IMPD*, 25, 1630024
Magee, M. R., Sim, S. A., Kotak, R., Maguire, K., & Boyle, A. 2019, *A&A*, 622, A102
Magee, M. R., Kotak, R., Sim, S. A., et al. 2016, *A&A*, 589, A89
Magee, M. R., Kotak, R., Sim, S. A., et al. 2017, *A&A*, 601, A62
Makarov, D., Prugniel, P., Terekhova, N., Courtois, H., & Vauglin, I. 2014, *A&A*, 570, A13
Maoz, D., Mannucci, F., & Nelemans, G. 2014, *ARA&A*, 52, 107
McClelland, C. M., Garnavich, P. M., Galbany, L., et al. 2010, *ApJ*, 720, 704
McCully, C., Jha, S. W., Foley, R. J., et al. 2014, *Natur*, 512, 54
McCully, C., Jha, S. W., Scalzo, R. A., et al. 2021, *ApJ*, arXiv:2106.04602
Narayan, G., Foley, R. J., Berger, E., et al. 2011, *ApJL*, 731, L11
Nomoto, K. 1982a, *ApJ*, 257, 780
Nomoto, K. 1982b, *ApJ*, 253, 798
Nomoto, K., Kamiya, Y., & Nakasato, N. 2013, IAU Symp. 281, *Binary Paths to Type Ia Supernovae Explosions 281* ed. R. Di Stefano, M. Orio, & M. Moe (Cambridge: Cambridge Univ. Press), 253
Nomoto, K., & Leung, S.-C. 2018, *SSRv*, 214, 67
Nomoto, K., Thielemann, F. K., & Yokoi, K. 1984, *ApJ*, 286, 644
Omar, A., Reddy, B. K., Kumar, T., & Pant, J. 2019, *BSRSL*, 88, 31
pandas development team, T 2020, pandas-dev/pandas: Pandas, latest, Zenodo doi:10.5281/zenodo.3509134
Pedregosa, F., Varoquaux, G., Gramfort, A., et al. 2011, *Journal of Machine Learning Research*, 12, 2825
Pettini, M., & Pagel, B. E. J. 2004, *MNRAS*, 348, L59
Phillips, M. M., Lira, P., Suntzeff, N. B., et al. 1999, *AJ*, 118, 1766
Phillips, M. M., Li, W., Frieman, J. A., et al. 2007, *PASP*, 119, 360
Pinto, P. A., & Eastman, R. G. 2000, *ApJ*, 530, 757
Poznanski, D., Prochaska, J. X., & Bloom, J. S. 2012, *MNRAS*, 426, 1465
Prentice, S., Maguire, K., Magee, M. R., & Deckers, M. 2020, *Transient Name Server Classification Report*, 2020-2685, 1
Rasmussen, C., & Williams, C. 2006, *Gaussian Processes for Machine Learning*, *Adaptive Computation and Machine Learning* (Cambridge, MA: MIT Press), 248
Riess, A. G., Filippenko, A. V., Li, W., et al. 1999, *AJ*, 118, 2675
Sahu, D. K., Tanaka, M., Anupama, G. C., et al. 2008, *ApJ*, 680, 580
Schlafly, E. F., & Finkbeiner, D. P. 2011, *ApJ*, 737, 103
Science Software Branch at STScI 2012, PyRAF: Python alternative for IRAF, *Astrophysics Source Code Library* ascl:1207.011
Seitenzahl, I. R., Ciaraldi-Schoolmann, F., Röpke, F. K., et al. 2013, *MNRAS*, 429, 1156
Shen, K. J., Kasen, D., Miles, B. J., & Townsley, D. M. 2018, *ApJ*, 854, 52
Sim, S. A., Fink, M., Kromer, M., et al. 2012, *MNRAS*, 420, 3003
Sim, S. A., Seitenzahl, I. R., Kromer, M., et al. 2013, *MNRAS*, 436, 333
Singh, M., Misra, K., Sahu, D. K., et al. 2018, *MNRAS*, 474, 2551
Skrutskie, M. F., Cutri, R. M., Stiening, R., et al. 2006, *AJ*, 131, 1163
Soker, N. 2015, *MNRAS*, 450, 1333
Sparks, W. M., & Stecher, T. P. 1974, *ApJ*, 188, 149
Srivastav, S., Smartt, S. J., Leloudas, G., et al. 2020, *ApJL*, 892, L24
Stehle, M., Mazzali, P. A., Benetti, S., & Hillebrandt, W. 2005, *MNRAS*, 360, 1231
Stritzinger, M. D., Hsiao, E., Valenti, S., et al. 2014, *A&A*, 561, A146
Szalai, T., Vinkó, J., Sárneczky, K., et al. 2015, *MNRAS*, 453, 2103
Tanikawa, A., Nomoto, K., & Nakasato, N. 2018, *ApJ*, 868, 90
Tanikawa, A., Nomoto, K., Nakasato, N., & Maeda, K. 2019, *ApJ*, 885, 103
Taubenberger, S. 2017, in *The Extremes of Thermonuclear Supernovae*, ed. A. W. Alsabti & P. Murdin (Berlin: Springer), 317
Thomas, R. C., Nugent, P. E., & Meza, J. C. 2011, *PASP*, 123, 237

- Tody, D. 1993, in ASP Conf. Ser. 52, *Astronomical Data Analysis Software and Systems II*, ed. R. J. Hanisch, R. J. V. Brissenden, & J. Barnes (San Francisco, CA: ASP), 173
- Tomasella, L., Cappellaro, E., Benetti, S., et al. 2016, *MNRAS*, **459**, 1018
- Tomasella, L., Stritzinger, M., Benetti, S., et al. 2020, *MNRAS*, **496**, 1132
- Turatto, M., Benetti, S., & Cappellaro, E. 2003, in *From Twilight to Highlight: The Physics of Supernovae*, ed. W. Hillebrandt & B. Leibundgut (Berlin: Springer), 200
- Valenti, S., Benetti, S., Cappellaro, E., et al. 2008, *MNRAS*, **383**, 1485
- Valenti, S., Pastorello, A., Cappellaro, E., et al. 2009, *Natur*, **459**, 674
- Van Der Walt, S., Colbert, S. C., & Varoquaux, G. 2011, *CSE*, **13**, 22
- Virtanen, P., Gommers, R., Oliphant, T. E., et al. 2020, *Nature Methods*, **17**, 261
- Wang, B., & Han, Z. 2012, *NewAR*, **56**, 122
- Wang, X., Filippenko, A. V., Ganeshalingam, M., et al. 2009, *ApJL*, **699**, L139
- Webbink, R. F. 1984, *ApJ*, **277**, 355
- Whelan, J., & Iben, I. J. 1973, *ApJ*, **186**, 1007
- Yamanaka, M., Maeda, K., Kawabata, K. S., et al. 2015, *ApJ*, **806**, 191
- Yaron, O., & Gal-Yam, A. 2012, *PASP*, **124**, 668
- Zackay, B., Ofek, E. O., & Gal-Yam, A. 2016, *ApJ*, **830**, 27